research
center
pharmaceutical
engineering

TU Graz

Hannes Bauer, BSc

An Investigation of Triple-Flighted Extruder Elements via SPH Simulation

MASTER'S THESIS

to achieve the university degree of

Diplom-Ingenieur

Master's degree programm: **Chemical- and Process Engineering**

submitted to

Graz University of Technology

Supervisor

Univ.-Prof. Dipl-Ing. Dr.techn. Johannes Khinast

Institute of Process and Particle Engineering

Technical Advisor

Dipl.-Ing. Josip Matić, BSc

Institute of Process and Particle Engineering

Graz, November 2016

Statutory Declaration

I declare that I have authored this thesis independently, that I have not used other than the declared sources/resources, and that I have explicitly marked all material which has been quoted either literally or by content from the used sources.

Graz, _____ _____

Date Signature

Eidesstattliche Erklärung[1]

Ich erkläre an Eides statt, dass ich die vorliegende Arbeit selbstständig verfasst, andere als die angegebenen Quellen/Hilfsmittel nicht benutzt, und die den benutzten Quellen wörtlich und inhaltlich entnommenen Stellen als solche kenntlich gemacht habe.

Graz, am _____ _____

Datum Unterschrift

[1] Beschluss der Curricula-Kommission für Bachelor-, Master- und Diplomstudien vom 10.11.2008; Genehmigung des Senates am 1.12.2008

Abstract

In recent years Hot Melt Extrusion (HME) with Twin Screw Extruders (TSE) became increasingly popular in the pharmaceutical industry, because of its potential to increase the bioavailability of drugs.

From the drug development stage to the production stage, TSE of different scales are used. The majority of the screws are double-flighted. However, some – especially in small scale TSE – are triple-flighted. Transferring the HME process from one stage to another makes it critical to know more about the extrusion behavior of triple-flighted elements.

Thus, the investigation and characterization of the flow behavior is necessary. The Smoothed Particle Hydrodynamics (SPH) simulation method has a record of performing well in that regard. This meshfree method allows for the simulation of flow around complex intermeshing and rotating geometries found in a TSE. Its particle nature is advantageous for the application of tracer methods to characterize mixing.

In this work, three conveying elements with various pitches and two kneading elements with different stagger angles were investigated. Their pressure characteristic, their power characteristic and their mixing behavior was determined and discussed. Furthermore, the obtained pressure- and power characteristic is compared with previously simulated double-flighted elements.

Kurzfassung

In den letzten Jahren wurde das Schmelzextrusionsverfahren mit Doppelschneckenextrudern für die pharmazeutische Industrie immer beliebter, weil damit eine höhere Bioverfügbarkeit von Wirkstoffen ermöglicht werden kann.

Von der Entwicklungsphase bis zur Produktionsphase werden Doppelschneckenextruder von unterschiedlicher Größe eingesetzt. Am öftesten wird dabei die zwei-gängige Schneckengeometrie verwendet. Manchmal, vor allem in Kleinstextrudern, ist die Geometrie jedoch drei-gängig. Um den Schmelzextrusionsprozess von einer Phase in die nächstgrößere zu übertragen, ist es notwendig mehr über das Extrusionsverhalten von drei-gängigen Schnecken zu wissen.

Also wird die Untersuchung und die Charakterisierung des Strömungsverhaltens in der Schnecke notwendig. Smoothed Particle Hydrodynamics (SPH) ist eine Simulationsmethode die dafür bereits in der Vergangenheit erfolgreich angewandt wurde. Ihr netzfreier Charakter erlaubt es die Strömung um die komplexe ineinandergreifende und rotierende Geometrie zu simulieren. Als Partikelmethode ist sie besonders vorteilhaft um das Mischverhalten mittels Tracer-Methoden zu bestimmen.

In dieser Arbeit wurden drei Förderelemente mit verschiedenen Steigungen und zwei Knetelemente mit unterschiedlichen Versatzwinkeln untersucht. Ihre Druck- und Leistungscharakteristik sowie das Mischverhalten wurden bestimmt und erläutert. Außerdem wurden die erhaltenen Druck- und Leistungscharakteristika mit vorherigen Simulationen zwei-gängiger Elemente verglichen.

Contents

List of Figures

List of Figures

Nomenclature

Abbreviations

1-D	One-dimensional
API	Active Pharmaceutical Ingredient
CFD	Computational Fluid Dynamics
DF	Double-flighted, bi-lobed
EoC	Equation of Continuity
EoS	Equation of State
HME	Hot Melt Extrusion
ME	Momentum Equation
SPH	Smoothed Particle Hydrodynamics
TF	triple-flighted, tri-lobed
TSE	Twin Screw Extruder
TSG	Twin Screw Granulation
WCSPH	Weakly Compressible Smoothed Particle Hydrodynamics

Greek Symbols

Δt	Discrete time-step	[s]

Δx	Particle spacing	[m]
δ	Density variation	
η	Fluid viscosity	[Pa s]
η_e	Pumping efficiency factor	
γ	Material constant for the EoS	
ρ	Fluid density	$[\mathrm{kg\,m^{-3}}]$
ρ_0	Reference density	$[\mathrm{kg\,m^{-3}}]$
σ	Standard deviation	
σ_0	Standard deviation for the completely unmixed state	

Indices

a	In reference to an individual particle a
ab	Indication of a vector difference between a particle a and a particle b
b	In reference to the set of particles surrounding a particle a
i	Refers to an individual sample box
z	Refers to the axial direction (z-direction).

Latin Symbols

$(F_{ab})^n$	Function in the artificial pressure term	
$\dot{V}$	Volumetric flow rate	$[\mathrm{kg\,m^{-3}\,s}]$
A_0, A_1, A_2	Dimensionless parameter describing the pressure characteristic	

A_{free}	Free cross-sectional area between barrel and screws	$[\mathrm{m}^2]$
B	Pre-factor in Tait's equation of state	[Pa]
B_0, B_1, B_2	Dimensionless parameter describing the power characteristic	
c_S	Speed of sound	$[\mathrm{m\,s}^{-1}]$
D	Barrel diameter	[m]
d	Channel depth	[m]
f, $\mathbf{f}$	mass specific body force	$[\mathrm{m\,s}^{-2}]$
f_z	Axial flow resistance force per mass	$[\mathrm{m\,s}^{-2}]$
g	Gap width, clearance distance	[m]
h	Smoothing Length	[m]
K	Number of samples	
k	Segregation exponent	
L	Length of screw elements	$[\mathrm{kg\,m}^{-3}]$
L_{char}	Characteristic length	[m]
M	Mixedness	
m	Mass	[kg]
M_z	Axial momentum	[N m]
N	Number of rotations	
n	Rotational velocity	$[\mathrm{s}^{-1}]$
P	Screw input power	[W]

p	pressure	[Pa]
$P^*_{DissNonAx}$	Dimensionless power not converted into throughput	
P^*_{Pump}	Dimensionless pumping power	
p_{bg}	Background pressure	[Pa]
R	Pre-factor in the artificial pressure term	$[\mathrm{m}^5\,\mathrm{kg}^{-1}\,\mathrm{s}^{-2}]$
r, $\mathbf{r}$	Distance, Position vector	[m]
Re	Reynolds Number	
Re_E	Characteristic Reynolds number for extruder screws	
S	Segregation	
S_0	Initial segregation	
t	Time	[s]
T_S	Pitch	[m]
U_{char}	Characteristic velocity	$[\mathrm{m}\,\mathrm{s}^{-1}]$
v	velocity	$[\mathrm{m}\,\mathrm{s}^{-1}]$
V_{free}	Free volume between barrel and screws	$[\mathrm{m}^3]$
v_{max}	Estimated maximum velocity	$[\mathrm{m}\,\mathrm{s}^{-1}]$
W	Smoothing kernel, Weighting function	[m]
x, $\overline{x}$	Concentration, mean concentration of tracer particles	

Mathematical Notation

$\boldsymbol{\phi}$	Vector notation

$\nabla\phi$	Nabla operator, first order partial differential in space
$\nabla_a W_{ab}$	Kernel derivation
$\overline{\phi}$	Spatially averaged quantity
ϕ^*	Refers to a dimensionless flow property
ϕ_a	Arbitrary fluid property of an individual particle a
ϕ_b	Fluid property of particles b surrounding particle a

1 Introduction

Co-rotating Intermeshing Twin-Screw Extruders (TSEs) have many applications in the food, rubber and polymer industry. Compared to its single screw counterpart – which is the most often used extrusion device – TSEs offer better mixedness of the processed material. Additionally, the intermeshing screw design leads to small gaps between the two screws, and between the screws and the surrounding barrel. As a result, TSEs exhibit a certain self-cleaning effect.

Usually, the screws consist of several sequentially arranged elements. This modular approach allows for elements to be designed for specific purposes – like conveying, mixing or kneading. Various screw configurations are possible, making extrusion with TSEs a flexible process. Since recently, TSEs are used in pharmaceutical manufacturing (e.g. Twin-Screw Granulation (TSG), Hot Melt Extrusion (HME)).

In HME polymer powder is introduced into the TSE, melted, homogenized, pressurized and pushed through a die. As a next step, several downstream operations (e.g. pelletizing) can be set to achieve a solid dosage form[31]. Looking closer at HME, the key advantages become apparent:

- HME can be used to create amorphous solid dispersions, and thus enhance the bioavailability of poorly soluble APIs[2].
- TSEs are continuously operated. Compared to traditional batch manufacturing, continuous manufacturing might shorten production time, produce steady-quality products and increase overall productivity.

Shorter process design times, adaptability of the HME process from lab-scale to production-scale or optimization during operation are desired. For this process simulation and engineering tools are needed. The development of such a tool is challenging:

- Depending on the process stage (development, pilot or production) the same process is carried out in TSEs of different scales. The barrel diameters might range from 8 mm to 50 mm.
- Screw configuration, screw geometry is likely different on all scales.
- The flow behavior of the polymer melt is often non-Newtonian. Its simulation remains laborious and intricate.

To simulate the HME process, Eitzlmayr, Koscher, and Khinast [7] used a one-dimensional (1-D) model. The model requires the input of empirical parameters that can be obtained via experiment or hydrodynamical simulation. This thesis concerns itself with the 3-D fluid dynamical simulation of five screw elements yielding the key input parameters for the above mentioned model. Additionally, the pumping, mixing and flow behavior is investigated.

Specifically, the screw elements of the NANO16 extruder (Leistritz, DE) with a triple-flighted geometry are investigated. When triple-flighted geometries are used it is mostly in smaller extruders. The bulk of extruder screws are double-flighted. This discrepancy further inhibits scalability. The investigated elements are:

- three conveying elements with different pitches (10 mm, 15 mm and 20 mm)
- two kneading elements with different stagger angles (30° and 60°)

For the simulation of the flow field Smoothed Particle Hydrodynamics (SPH) is used. In this method the fluid domain is discretized by particles, which behave according to the laws of hydrodynamics, and not by a mesh as in conventional Computational Fluid Dynamics (CFD). This makes SPH a well suited method for the complex rotating geometry of extruder elements.

Chapter 2 is dedicated to the process of HME and the various mechanisms and phenomena associated with its hydrodynamics. In Chapter 3, current simulation methods, the details of SPH and its application to our elements are shown. In Chapter 4 the simulation results of the investigated elements are presented and discussed. Properties of the triple-flighted geometry and the more widely used double-flighted geometry are compared. Concluding remarks can be found in Chapter 5.

2 Hot Melt Extrusion

Here, an overview of the extrusion process and the nature of triple-flighted screw elements is given. Its goal is to describe underlying phenomena and draw comparisons between different screw elements. Furthermore, the theory to quantify and characterize different screw elements is explained and put into context.

2.1 Hot Melt Extrusion using The Co-rotating Intermeshing Twin-screw Extruder

Main parts of a TSE are the horizontally aligned screws (consisting of several elements) and their surrounding barrels (Figure 2.2). Both screws are rotating in the same direction (i.e. co-rotating). The screw elements are designed for specific purposes: Conveying elements induce axial flow and build up pressure, kneading elements are primarily responsible for dispersive mixing and mixing elements for distributive mixing (more about mixing in Section 4.2).

Individual screw configurations specifically tailored to the product are possible. The resulting process zones depend heavily on the screw configuration, but also on the material parameters (e.g. viscosity) and process parameters (e.g. rotational velocity). This makes it hard to identify exactly where individual process zones begin or end by looking at the screw configuration alone. Nonetheless, process zones are similar for a lot of HME processes (Figure 2.1) and are associated with a particular combination of elements:

- Powder-/Melt-Conveying Zone: In this zone solid powder is introduced into the TSE. Conveying screws compress it and remove the air.

A combination of heat (applied at the barrel) and mechanical shear (generated by conveying and kneading elements) cause the powder to plastify and become a viscous polymer melt. Optionally, after the powder has fully melted, a secondary input stream (e.g. API) may be added.

- Kneading Zone: At the beginning of the kneading zone the pitch of the conveying screw is decreased to compensate for the lack of pressure build-up in the following elements. The following elements are kneading elements. Their primary purpose is to break up agglomerates.
- Mixing Zone: The mixing zone starts with a conveying element, is followed by a conveying element of lesser pitch, a mixing element and a backwards-conveying element. The backwards conveying element ensures a high residence time in the mixing zone. Axial openings in the flights are characteristic for mixing elements. They introduce additional flow streams, which later cross and enhance distributive mixing.
- Degassing Zone: The degassing zone is necessary for removing any volatile gases. It is located between two fully filled zones and normally consists of conveying elements with a high pitch to decrease the filling level. This increases the free surface of the melt and ensures efficient degassing.
- Discharge Zone: Conveying elements of decreasing pitch are mounted next to each other. The pressure build-up has to be high enough to press the material through the die.

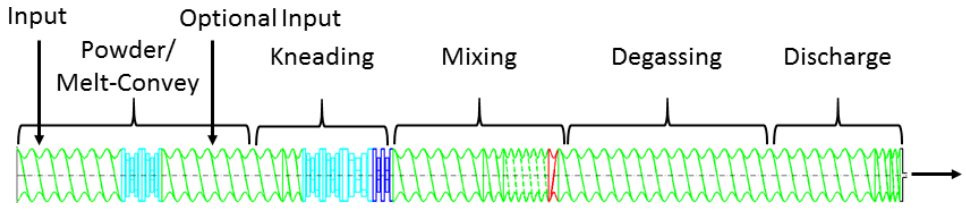

Figure 2.1: Axial view of a typical screw configuration with process zones indicated. (from a 1D model[9])

2.2 Cross Sectional Profile of Triple-Flighted Geometries

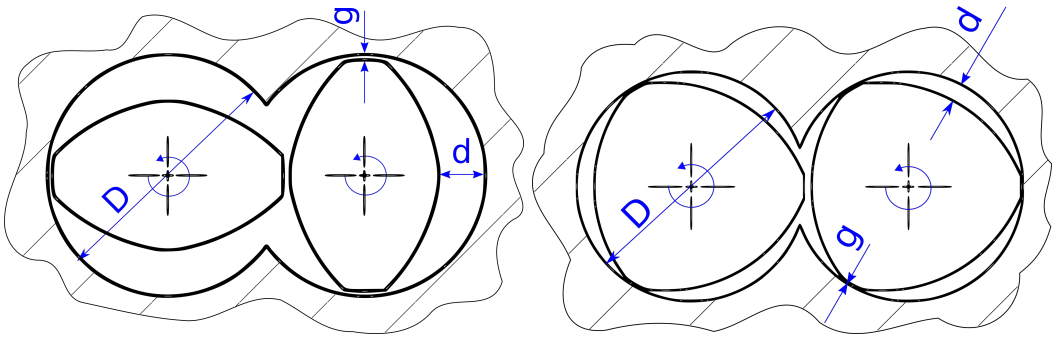

(a) Double-flighted geometry (b) Triple-flighted geometry

Figure 2.2: Schematic cross-sectional profiles of double-flighted and triple-flighted co-rotating screw geometries with key measurements (barrel diameter D, channel depth d and gap width g).

Ideally, intermeshing screws are kinematically designed in such a way, that during the engagement of flank and channel they are touching each other. This way, adhering residual material is scraped off of the screws and a self-cleaning effect sets in. However, for practical purposes a small gap is necessary. To maximize the self-cleaning effect, the gap should be as small as possible. Usually, the double-flighted geometry is used (Figure 2.2a). However, for the lab-scale extruder NANO16 a triple-flighted geometry (Figure 2.2b) is preferred. The triple flighted screw geometry has a greater cross-sectional area than the double-flighted screw geometry. This leaves less room for the processed material and therefore a lower mass throughput can be achieved. Contrary to TSEs operating at the production-scale, lab-scale TSEs are typically used in trial and error experiments in which low mass throughput is desired. This limits the loss of the used material, allows for more test runs and for lower experimental costs.

TSEs at the production-scale might still operate with a double-flighted geometry. However, with the triple-flighted geometry three flanks instead of two are engaging. The difference in flights complicates the transfer of

the process to larger scales. The use of triple-flighted elements leads to a higher pressure build-up capability and more energy input (as shown later on in the results). Rules of geometrical similarity can not be applied any longer and intermittent scale-up steps are necessary. A characterization of TSE screws – especially of their hydrodynamical behavior – allows for comparability between different scales and cross-sectional profiles.

2.3 Hydrodynamical Screw Characterization via Dimensionless Parameters

According to Pawlowski [25] the flow in fully filled single-screw extruders is defined by three independent dimensionless groups: The throughput number $\dot{V}^*$, the pressure number Δp^* and the power number P^* (Eqn. 2.1-2.3). In these, $\dot{V}$ is the volume flow rate, n the rotational speed, D the barrel diameter, Δp the pressure difference, L the screw length and P the power consumption of the process. Pawlowskis findings are also relevant for TSEs.[14].

$$\dot{V}^* = \frac{\dot{V}}{nD^3} \tag{2.1}$$

$$\Delta p^* = \frac{\Delta p D}{\eta n L} \tag{2.2}$$

$$P^* = \frac{P}{\eta n^2 L D^2} \tag{2.3}$$

The pressure characteristic (Δp^* as a function of $\dot{V}^*$) as well as the power characteristic (P^* as a function of $\dot{V}^*$) depend on three points:

- The rheological behavior of the fluid: Non-Newtonian fluids complicate the characterization of screw elements. However, for Newtonian fluids the pressure characteristic as well as the power characteristic are linear. Thus, a fluid with constant viscosity is used for the characterization.

- The geometrical dimensions: The outer dimensions (like length and barrel diameter) are considered in the dimensionless groups. The dependency of more detailed geometrical parameters (like gap width or pitch) remains.
- The extruder Reynolds number Re_E (Eqn. 2.6): Due to the high viscosity of polymer melts, viscous forces are much bigger than inertial forces. Under these so-called creeping flow conditions inertial terms play a negligible role. Eqn. 2.4 shows the dimensionless form (brackets indicate dimensionless groups) of the incompressible isothermal Navier-Stokes equation, where L_{char} is a characteristic length, U_{char} a characteristic velocity and $Re = U_{char} L_{char} / \nu$ the local Reynolds number.

$$Re \left(\frac{L_{char}}{U_{char}^2} \frac{\mathrm{D}\mathbf{v}}{\mathrm{D}t} \right) = - \left(\frac{L_{char}^2 \nabla p}{\eta U_{char}} \right) + \left(\frac{L_{char}^2 \nabla^2 \mathbf{v}}{U_{char}} \right) \tag{2.4}$$

  The left-hand side (LHS) of the dimensionless Navier-Stokes equation vanishes for small Re, leading to the Stokes equation:

$$\nabla p = \eta \nabla^2 \mathbf{v} \tag{2.5}$$

  Eqn. 2.5 is now independent of Re. As a consequence the flow is now also independent from Re_E. This creeping flow assumption holds true for $Re_E \leq 10$[6].

$$Re_E = \frac{n D^2 \rho}{\eta} \tag{2.6}$$

To summarize, for Newtonian creeping flows of fully filled screws the pressure and power characteristic are linear and independent of the viscosity and the rotational speed (i.e. Re_E). It is only dependent on the screw geometry.

Because of its linearity the pressure characteristic is defined by two parameters, the axes intercepts A_1 and A_2 and a corresponding equation (Figure 2.3a, Eqn. 2.7). In a similar fashion B_1 and B_2 for the description of the power characteristic are found (Eqn. 2.8 , Figure 2.3b).

$$\Delta p^* = -\frac{A_2}{A_1} \dot{V}^* + A_2 \tag{2.7}$$

$$P^* = -\frac{B_2}{B_1}\dot{V}^* + B_2 \tag{2.8}$$

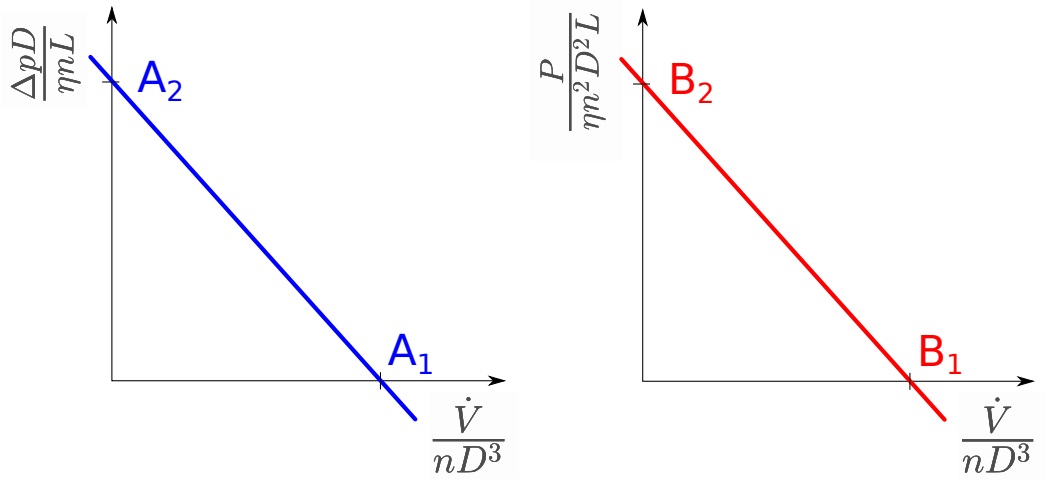

(a) Pressure characteristic (b) Power characteristic

Figure 2.3: Schematic representation of the linear relationship between pressure build-up and throughput, as well as power-input and throughput.

Extruders exhibit all the traits that rotodynamic pumps do. That is, mechanical rotational energy goes in resulting in a conveyed fluid. The difference is, that pumps have the primary purpose of conveying fluid, whereas extruders have many different tasks. The usual laws can be applied to characterize the pumping power of an extruder:

$$P^*_{Pump} = \dot{V}^* \times \Delta p^* \tag{2.9}$$

With the consideration of Eqn. 2.7 a quadratic relationship for the pumping power of a given screw element is found:

$$P^*_{Pump} = \dot{V}^* \left(-\frac{A_2}{A_1}\dot{V}^* + A_2 \right) \tag{2.10}$$

Not all of the mechanical input power is converted into pumping. The rest is either converted to non-axial flow or dissipated:

$$P^*_{DissNonAx} = P^* - P^*_{Pump} \tag{2.11}$$

Again, a quadratic relationship can be found by inserting Eqn. 2.8 and Eqn. 2.10:

$$P^*_{DissNonAx} = \frac{A_2}{A_1}\dot{V}^{*2} - \left(A_2 + \frac{B_2}{B_1}\right)\dot{V}^* + B_2 \tag{2.12}$$

An efficiency factor η_e can be defined. η_e shows how much pumping power is generated relative to the entire power input. It is expected to be relatively small compared to actual pumps:

$$\eta_e = \frac{P^*_{Pump}}{P^*} \tag{2.13}$$

2.4 Mixing Mechanisms and Evaluation

Turbulence is the most efficient mixing mechanism, but due to high viscosities of polymer melts it is not present in HME. Mixing in an extruder takes place in a creeping flow environment. Generally, it can be differentiated between two types of mixing with different characteristics and mechanisms (Figure 2.4)[24]:

- Distributive mixing displaces agglomerates homogeneously over the entire fluid volume. This happens through the folding of stream lines and movement of entire fluid zones. This task is best achieved by mixing elements.
- Dispersive mixing is defined as the breaking-up of agglomerates. It is heavily dependent on shear forces. The results are mixed zones at a smaller scale. This is the primary goal of kneading elements.

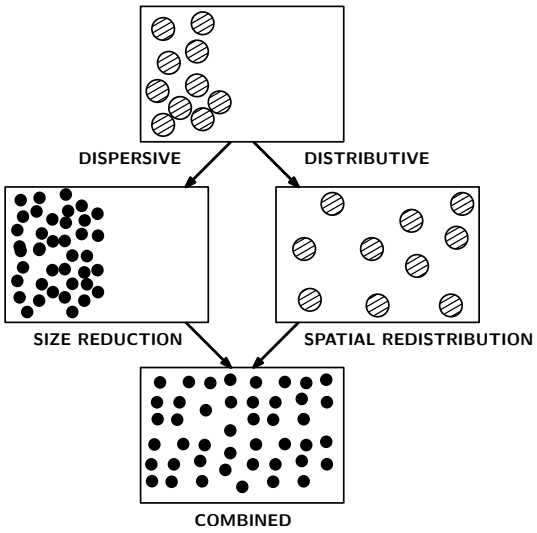

Figure 2.4: Difference between distributed and dispersive mixing. (Source: A. Troiss, 2016)

Both mixing types are needed to consistently achieve good mixtures at relevant (i.e. sufficiently small) scales. Furthermore, mixing in a HME process usually takes place between several compounds. These compounds may be in different states, and therefore in different phases. In theory, the following binary systems may be mixed:

- Solid-Liquid Systems: Granules are added to the polymer melt and need to be distributed and dispersed. Complex matters like granule break-up and formation need to be considered.
- Liquid-Liquid systems: Two viscous melts are added. The interfacial tension, different fluid properties, miscibility or immiscibility, drop formation are just a few things that influence the mixing behavior.

These complex mechanisms are tasks for sophisticated multi-phase simulations. In this work, the hydrodynamical simulation considers the single phase flow in an extruder element. Thus, only distributive mixing can be investigated. The employed tracer method marks several particles (moving calculation nodes in SPH) as a tracer. The marking has no influence on the flow field.

The (un-)mixedness of a particle system is often indicated by the standard deviation σ from an average mass concentration $\overline{x}$ of K samples (Eqn. 2.14). The samples should be statistically representative of the particle system. The size of all samples should be equal to the scale at which homogeneity is desired. This way, σ can be used as a mixedness quality indicator.

$$\sigma = \sqrt{\frac{1}{K-1}\sum_{i=0}^{K}(x_i - \overline{x})^2} \tag{2.14}$$

A dimensionless representation can be found by normalizing σ with σ_0 – the standard deviation in a completely unmixed state[15] (Eqn. 2.15). At the beginning of the mixing process the Segregation will be a maximum ($S \approx 1$). With time, however, material is distributed more evenly, σ decreases, yielding a better mixture ($S \ll 1$).

$$S = \frac{\sigma}{\sigma_0} = \frac{\sigma}{\overline{x}(1-\overline{x})} \tag{2.15}$$

$$S = S_0 e^{-kN} \tag{2.16}$$

$$M = 1 - S = 1 - S_0 e^{-kN} \tag{2.17}$$

To capture the timely evolution of S an exponential model is used (Eqn. 2.16). In this equation S_0 is limited in its importance as it symbolizes the state of initial segregation, and is therefore dependent on the used tracer. More interesting is the segregation exponent k as a measure for the decrease in segregation per rotations N. Alternatively to S, the Mixedness M can be defined (2.17). M approaches zero for the demixed state and unity for the completely mixed state.

3 Hydrodynamic Simulation

This chapter deals with the simulation part of the thesis. It will give an overview of conventional extruder simulations with other methods and compare them to the method used. The theoretical background for SPH is provided. Lastly, the application of the method to extrusion elements is described and discussed.

3.1 Hydrodynamic Simulation for Extrusion

Many attempts at predicting the flow situation in TSE have been made. The books from Kohlgrüber [14] and Rauwendaal [27] give a good overview of 2-D and 3-D methods for extruder simulation.

Here are a few examples of twin screw extruder simulation. These examples mainly use conventional CFD methods in which the fluid domain is spatially discretized. It should be mentioned, that the list is by no means complete, nor does it aim to be:

- R.A. Lai-Fook, A. Senouci and Smith [26] investigated the flow in a double flighted conveying element. They used the approach of unwinding the screw channel, therefore reducing the problem to a 2-D, isothermal, non-Newtonian, steady state flow. Only, the flow in the screw channel was investigated; the intermeshing region and leakage streams in the gap were not resolved.
- Cheng and Manas-zloczower [3] investigated the flow and mixing behavior of triple-flighted elements. They simulated a 3-D, isothermal, non-Newtonian flow. The intermeshing region was considered. However, gaps were not resolved. The mixing behavior was characterized with a particle tracking method.

- Hetu and Ilinca [12] used a stationary mesh which covers the fluid region as well as the solid part. The screws were treated as an immersed rotating boundary. Resulting boundary conditions were enforced on the stationary mesh. With this method, the flow fields in double-flighted conveying and mixing elements were investigated. The flow in the gap region was resolved.
- Sobhani et al. [29] coupled the energy and the momentum equation to simulate the thermal behavior of a non-Newtonian flow in a double flighted conveying element. Gap regions were fully resolved.
- Sarhangi Fard and Anderson [28] used a mapping method to investigate distributive mixing. With this method the particle concentration in a volume grid is measured. The grid deforms with each time-step and particles are constantly reassigned.

With complex rotating geometries, flow simulation with CFD tools becomes a challenging task. Usually, multiple meshes or sophisticated re-meshing methods are needed. On the other hand, SPH is especially useful for handling moving boundaries[7], and there is no need for a mesh. It, being a particle method, naturally incorporates particle tracer methods (e.g. mapping method). Furthermore, while not relevant for this thesis, SPH can handle free surface flows[19] which occur in HME when screw elements are only partially filled.

3.2 Smoothed Particle Hydrodynamics

3.2.1 Introduction

Initially, SPH was developed for astrophysical applications[11]. Examples include the simulation of star formation or galaxy merging[30]. A less accurate, but faster version is used in the area of computer animation[23]. Engineering applications are spread out over various disciplines like coastal engineering [21], environmental engineering (e.g. flooding due to rock slides [32]) or metal forming [4].

Smoothed Particle Hydrodynamics is a Lagrangian method for simulating the flow of fluids. The fluid is represented by calculation nodes (i.e. particles) that move through space. Therefore, the method can be considered as a meshless alternative to conventional CFD codes.

The main drawback of the method is the comparatively high computational effort needed for applications that require a high spatial resolution. Therefore, in the past SPH has not been developed as intensively as CFD methods. However, for some applications (e.g. free surface flows like mud slides) SPH looks very promising and this is currently driving further research.

Following the ideas of Eitzlmayr and Khinast [6], who were the first to use SPH for the simulation of TSE elements, the open source code LIGGGHTS ® from the CFDEM® project is used.

3.2.2 Kernel Estimation - The Basic Principle of SPH

The particle-based nature of SPH allows fluid properties of a single particle to be estimated from its neighbors. For this purpose a smoothing function, a so-called Kernel, is used: An arbitrary flow property ϕ of a particle a may be estimated from the surrounding particles b via the Kernel function $W(r,h)$ (Eqn. 3.1,[20]). $W(r,h)$ acts as a Gaussian-like weighing function. Therefore, particles nearer to a contribute more to the estimate.

$$\phi_a(\mathbf{r}) = \int W(r_{ab},h)\phi_b(\mathbf{r_b})\,\mathrm{d}\mathbf{r_b}. \tag{3.1}$$

Ideally, the weighing function $W(r,h)$ is a Gaussian bell curve. However, to save computational time a cubic spline (Eqn. 3.2) function is used. The smoothing length h marks the part of the computational domain where $W(r,h)$ is active (Figure 3.1). Particles outside of a range of $2h$ do not contribute to the estimate at all.

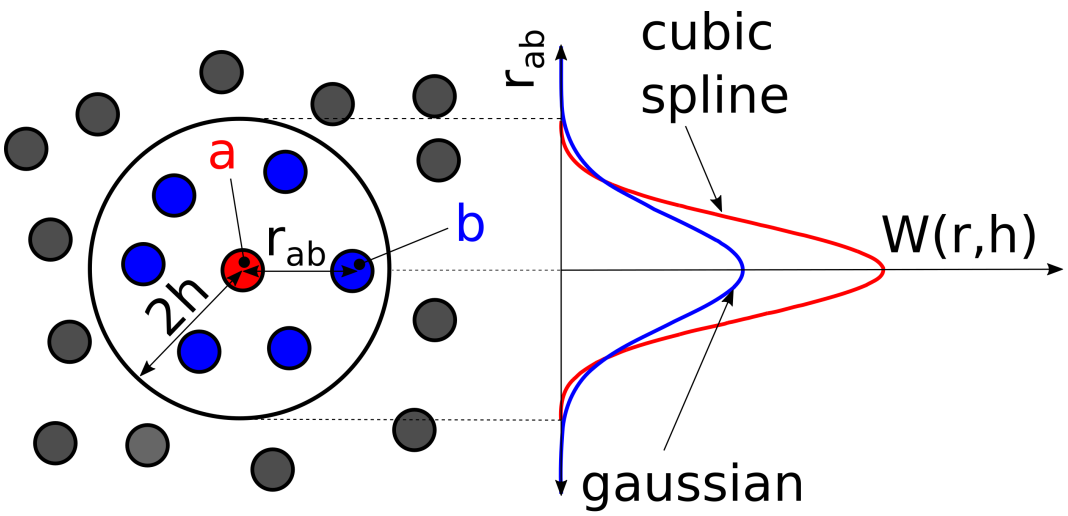

Figure 3.1: The principle of Kernel estimation

$$W(\mathbf{r},h) = \frac{1}{\pi h^3}\begin{cases} 1 - \frac{3}{2}\left(\frac{r_{ab}}{h}\right)^2 + \frac{3}{4}\left(\frac{r_{ab}}{h}\right)^3 & \text{if } 0 \leq \frac{r_{ab}}{h} < 1 \\ \frac{1}{4}\left(2 - \frac{r_{ab}}{h}\right)^3 & \text{if } 1 \leq \frac{r_{ab}}{h} < 2 \\ 0 & \text{if } 2 \leq \frac{r_{ab}}{h} \end{cases} \tag{3.2}$$

The integral term used for estimating arbitrary fluid properties (Eqn. 3.1) is approximated by a summation term:

$$\phi_a(\mathbf{r}) = \sum_b m_b \frac{\phi_b}{\rho_b} W(r_{ab}, h) \tag{3.3}$$

Eqn. 3.3 is used to bring the governing equations of fluid dynamics into a form well suited for numerical computation[20].

For isothermal flows these are the equation of continuity (EoC) and the momentum equation (ME):

$$\frac{\mathrm{D}\rho}{\mathrm{D}t} + \rho(\nabla \cdot \mathbf{v}) = 0 \tag{3.4}$$

$$\rho \frac{\mathrm{D}\mathbf{v}}{\mathrm{D}t} = -\nabla p + \eta \nabla^2 \mathbf{v} + \rho \mathbf{f} \tag{3.5}$$

The EoC (Eqn. 3.4) ensures mass conservation. The ME (Eqn. 3.5) relates the motion of fluid elements to applied forces (like pressure gradients ∇p, viscous forces $\eta \Delta \mathbf{v}$ or body forces $\mathbf{f}$ (e.g. gravity).

3.2.3 Weakly Compressible SPH

In this thesis the fluid is regarded as incompressible. However, SPH was developed for compressible media. The solution scheme relies on an Equation of State (EoS) to link density and pressure. By setting the speed of sound c_S and selecting an appropriate EoS the density variation ($\delta = \Delta\rho/\rho$) can be controlled and only slight compressibility is permitted. With this approach, which is termed Weakly Compressible SPH (WCSPH) [20], accurate results can be obtained.

c_S is a quantity that does not effect the ME (Eqn. 3.11) directly. However, it is a property in the EoS (Eqn. 3.12). The minimum required speed of sound to guarantee a small density variation can be estimated by inserting the EoS into the momentum equation and comparing the order of magnitude of the terms as shown by Morris, Fox, and Zhu [22]. The resulting (near)-incompressiblity criteria are the subsonic condition (Eqn. 3.6), the viscous condition (Eqn. 3.7), and the body force condition (Eqn. 3.8).

$$c_S^2 \geq \frac{v_{max}^2}{\delta} \tag{3.6}$$

$$c_S^2 \geq \frac{\eta v_{max}}{\rho L_{char} \delta} \tag{3.7}$$

$$c_S^2 \geq \frac{f_{max} L_{char}}{\delta} \tag{3.8}$$

A high speed of sound normally leads to a small time-step (see Section 3.2.8). Therefore, the chosen speed of sound is always a trade-off between density variation (accuracy) and computational effort.

3.2.4 Equation of Continuity

In SPH each particle is assigned a constant mass m. Therefore, mass conservation is satisfied, if the number of particles in the computational domain does not change. The other purpose of the EoC is to calculate the density at local points. Density can be either estimated as an absolute value or as a density change. The latter option offers some advantage in time stepping and is used here [20]:

$$\frac{d\rho_a}{dt} = \sum_b m_b \mathbf{v_{ab}} \nabla_a W_{ab} \tag{3.9}$$

For the calculation of the density change the mass of the surrounding particles m_b and their velocities relative to the particle a – namely $\mathbf{v}_{ab}$ – are required. This follows directly from the application of a derivation operation to Eqn. 3.3 for the density ρ. The velocity term is a result of the derivation of the Kernel function $W(r_{ab}, h)$. Please note, that the only needed derivation operation in Eqn. 3.9 is applied to the known Kernel function.

3.2.5 Momentum Equation

Initially, Monaghan [20] used a momentum equation of the following form:

$$\frac{d\mathbf{v_a}}{dt} = -\sum_b m_b \left(\frac{p_a}{\rho_a^2} + \frac{p_b}{\rho_b^2} + \Pi_{ab} \right) \nabla_a W_{ab} + \mathbf{f_a} \tag{3.10}$$

In this the term $p_a/\rho_a^2 + p_b/\rho_b^2$ represents the pressure gradient, $\mathbf{f_a}$ is an arbitrary body force and Π_{ab} is the viscous term. Morris, Fox, and Zhu [22] showed that the original formulation of the viscous term is inadequate for flows at low Reynolds numbers and proposed a different term. Later, Monaghan [17] extended this form to further increase the numerical stability:

$$\frac{d\mathbf{v_a}}{dt} = \overbrace{-\sum_b m_b \left(\frac{p_a}{\rho_a^2} + \frac{p_b}{\rho_b^2} \underbrace{+R(F_{ab})^n}_{\text{artificial pressure}} \right) \nabla_a W_{ab}}^{\text{pressure term}} \underbrace{+\sum_b \frac{m_b(\eta_a + \eta_b)\mathbf{v}_{ab}}{\rho_a \rho_b} \left(\frac{1}{r_{ab}} \frac{\partial W_{ab}}{\partial r_a} \right)}_{\text{viscous term}} + \mathbf{f_a} \quad (3.11)$$

Eqn. 3.11 is the equation that is implemented in the used software code. The pressure term includes – contrary to the differential form of the Navier-Stokes equations – the absolute pressure and not the gradient. The artificial pressure term acts as a stabilizing term. It is big when the distance between particles is below the predefined particle spacing Δx and decreases significantly if the particle distance approaches two smoothing lengths h. The factor R ensures that the pressure terms and the artificial pressure terms are of similar magnitude. It is a function of pressure and density. The viscous term is the formulation proposed by Morris, Fox, and Zhu [22].

3.2.6 Equation of State

To link density changes to pressure changes Tait's Equation of State (EoS) is used:

$$p = B \left(\left(\frac{\rho}{\rho_0} \right)^\gamma - 1 \right) + p_{bg} \quad (3.12)$$

In this, ρ is the current density, ρ_0 the reference density, and γ a material parameter which is not important for steady state simulations with WCSPH. The pre-factor B was calculated according to Eqn. 3.13:

$$B = \frac{c_S^2 \rho_0}{\gamma} \tag{3.13}$$

Zones with negative pressure cause stability problems in SPH. To avoid this, Tait's equation of state was extended with a background pressure p_{bg}.

3.2.7 Tensile Instability

A common occurance in SPH is the unphysical clustering of particles which results in void regions. This happens when particles experience a negative pressure – a tensile stress – and is therefore called tensile instability. Tensile instability is a numerical problem that stems directly from the principle of kernel estimation. Liu and Liu [16] detail a number of solutions for this problem (e.g. using different kernels). Extruder simulations are especially prone to local pressure variations up- and downstream of the flanks and in the gaps between barrel and screw. To enhance the stability of the simulation a background pressure p_{bg} is added to the equation of state.

3.2.8 Time Stepping

At the beginning of a generic time step t the initial particle velocity $\mathbf{v_a}(\mathbf{t})$, the forces acting on the particle $\mathbf{f_a}(t)$, the density change $\dot{\rho}_a(t)$, the pressure $p_a(t)$ and the position of the particles $\mathbf{r_a}(t)$ need to be known. To evolve the fluid properties over time a two-step procedure (a modified velocity-verlet scheme) is used[10]:

- First, the velocity and the density are evolved to the half step (Eqn. 3.14-3.15). Then the position of the particles at the next step is calculated (Eqn. 3.15). Additionally, the velocity at the full step is estimated (Eqn. 3.17).

$$\mathbf{v_a}(t + \frac{1}{2}\Delta t) = \mathbf{v_a}(t) + \frac{\Delta t}{2}\frac{d\mathbf{v_a}}{dt}(t) \tag{3.14}$$

$$\rho_a(t + \frac{1}{2}\Delta t) = \rho_a(t) + \frac{\Delta t}{2}\frac{d\rho_a}{dt}(t) \tag{3.15}$$

$$\mathbf{r_a}(t + \Delta t) = \mathbf{r_a}(t) + \Delta t\mathbf{v_a}(t + \frac{1}{2}\Delta t) \tag{3.16}$$

$$\tilde{\mathbf{v}}_\mathbf{a}(t + \Delta t) = \mathbf{v_a}(t) + \Delta t\frac{d\mathbf{v_a}}{dt}(t) \tag{3.17}$$

- Secondly the remaining fluid properties at the full step are calculated (Eqn. 3.18-3.20). Here, the governing equation of SPH shown in previous sections are used. Please, note that for accuracy reasons the previously calculated $\tilde{\mathbf{v}}_\mathbf{a}(t + \Delta t)$ is used. Hereafter, the density and (real) velocity can be evolved (Eqn. 3.21-3.22).

$$\frac{d\rho_a}{dt}(t + \Delta t) \tag{3.18}$$

$$p_a(t + \Delta t) \tag{3.19}$$

$$\frac{d\mathbf{v_a}}{dt}(t + \Delta t) \tag{3.20}$$

$$\rho_a(t + \Delta t) = \rho_a(t + \frac{1}{2}\Delta t) + \frac{\Delta t}{2}\frac{d\rho_a}{dt}(t + \Delta t) \tag{3.21}$$

$$\mathbf{v_a}(t + \Delta t) = \mathbf{v_a}(t + \frac{1}{2}\Delta t) + \frac{\Delta t}{2}\frac{d\mathbf{v_a}}{dt}(t + \Delta t) \tag{3.22}$$

The criteria for choosing a sufficiently small time step are the Courant-Friedrich-Lewy criterion (Eqn. 3.23), the viscous condition (Eqn. 3.24), and the body force condition (Eqn. 3.25).[1][9][22]:

$$\Delta t < 0.25\frac{h}{c_S} \tag{3.23}$$

$$\Delta t < 0.125\frac{\rho h^2}{\eta} \tag{3.24}$$

$$\Delta t < 0.25\sqrt{\frac{h}{f_{max}}} \tag{3.25}$$

As can be seen the smoothing length h heavily influences the needed time-step. Thus, spatial resolution and the time resolution are coupled.

3.2.9 Boundary Treatment

In SPH there are a few methods on how to achieve appropriate particle-wall interactions. Monaghan and Kajtar [18] give a good overview. Screw elements are an interesting case in terms of boundary treatment. The geometry features concave and convex surfaces, narrow gaps between the screws, and between screw and barrel. Furthermore, the geometry is rotating. The standard method in SPH is to treat solid surfaces as solid particles. This method is used for the stationary boundaries that the barrel provides. Eitzlmayr, Koscher, and Khinast [7] show how to model moving solid boundaries in a twin-screw extruder with a wall force model. The main advantage of this model is that it can be used for arbitrarily shaped boundaries. Additionally, a repulsion force is included, which acts at very small distances, and forces the wall to be impenetrable.

3.3 Simulation Approach

3.3.1 Basic Set-Up

In total, 28 simulation runs were carried out. Each simulation run consisted of an intermeshing pair of screws (Figure 3.4) and a surrounding barrel (Figure 2.2b).

Initially, particles in the fluid domain are set on a lattice with defined particle spacing Δx_{init}. When particles are set in close proximity to the boundary wall, the resulting excessive forces may destabilize the entire system. Therefore, it is better to initially set the particles on a denser lattice

($\rho_{init} > \rho$) with decreased particle spacing ($\Delta x_{init} < \Delta x$) and to keep some distance to the boundary wall. As the simulation progresses, the dense particle lattice relaxes, the desired particle spacing Δx and density ρ are achieved, and the fluid volume is fully filled.

When polymer melt flows along the extruder length it is met with some resistance. This resistance takes the form of a pressure difference. The pressure build-up of the rotating screw needs to exceed the pressure difference, otherwise the flow direction is inversed. In these simulations, instead of a pressure loss, the particles are decelerated by an equivalent specific force f_z, which opposes the conveying direction (Figure 3.2). The throughput is a result of f_z and the rotational velocity n of the screws. At the flush sides of the screw periodic boundary conditions are set (Figure 3.2). If a particle leaves on one side it is instantly created at the other, and retains its flow properties.

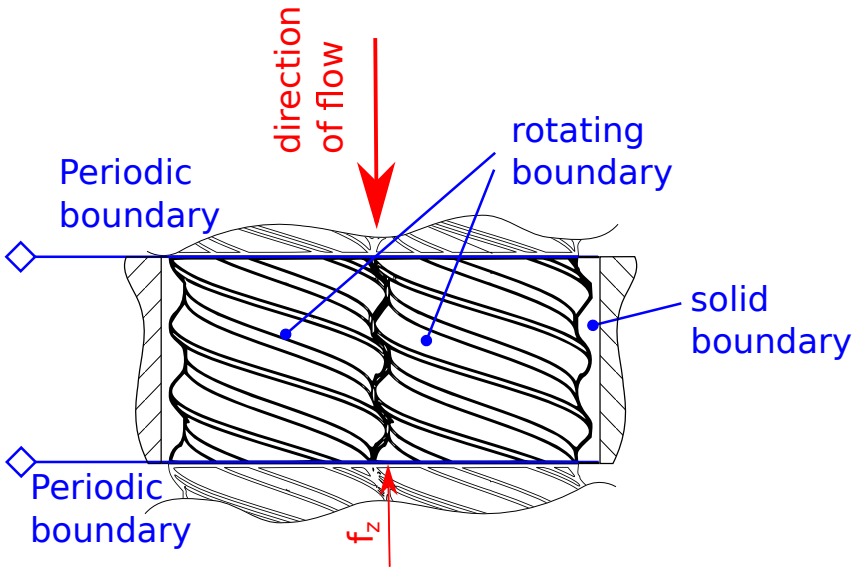

Figure 3.2: Schematic drawing of the simulation setup.

A lot of the properties in the dimensionless groups $\dot{V}^*$, Δp^* and P^* are given by the screw geometrics or the fluid material data. The rest are results

gained from the simulation. They are time averaged – not including the unsteady starting period:

- The throughput is calculated from the averaged axial velocity:

$$\dot{V} = A_{free}\overline{v}_z \tag{3.26}$$

- The flow resistance in this simulation takes the form of a specific force opposing the flow direction:

$$\Delta p = L\rho f_z \tag{3.27}$$

- The power input via the twin screws is calculated from their averaged axial moment:

$$P = 2\pi n(\overline{M}_{z1} + \overline{M}_{z2}) \tag{3.28}$$

To track the mixing behavior a total of five revolutions are simulated (although in a few simulation runs ten revolutions were needed). For all simulations a steady state (i.e. little to no variation in throughput) could be observed at least after a half turn. At this point various tracers are set:

- Axial tracer: Here, the screw element is divided into the equally sized parts along its cross section. Therefore, axial mixing can be investigated (Figure 3.3a).
- Cross tracer: The screw element is divided in a left and a right part. Mixing from one screw to another can be investigated (Figure 3.3b).
- Quarter tracer: The Quarter tracer is a combination of the Axial tracer and the Cross tracer. Both, axial mixing and cross mixing are shown by this tracer (Figure 3.3c).

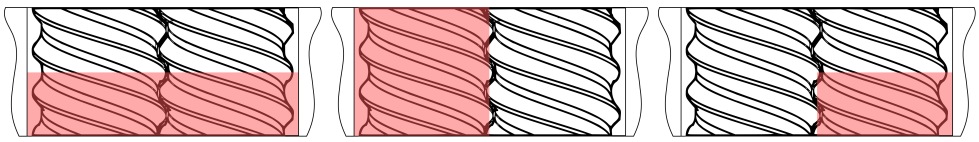

(a) Axial (b) Cross (c) Quarter

Figure 3.3: Different tracer settings used for the simulation.

The simulation domain was divided into a lattice of equal sized cubic boxes. The concentration of tracer particles in the boxes was evaluated during

the simulation run. Each box is regarded as a sample out of which the segregation S for a particular time-step is calculated (Eqn. 2.15). Viewed over the entire simulation run a segregation-rotation curve captures the mixing dynamic. A kinetic model, fitted to S, delivers the segregation exponent k and quantifies the mixing behavior (Eqn. 2.16). The box sizes were chosen to be 0.5 mm and 1 mm. Depending on the size, the fact that sometimes boxes are cut by the screw or barrel geometry, and density fluctuations the particle count in the boxes deviates from the theoretical estimate. However, to ensure equal sample sizes only small deviations are accepted (0.5 mm: 27 ± 2 particles, 1 mm: 296 ± 2 particles), the rest are ignored. Naturally, this procedure diminishes the sample number. 1 mm-boxes are effected more, because they are more easily cut by the solid geometries. In fact, in a simulation of the element C15 only around 30 boxes are accepted, which represent only about 1 % of the fluid domain. In comparison, the accepted 0.5 mm-boxes represent approximately 25 % of the fluid volume. Therefore, 1 mm-boxes are not statistically relevant, and are not considered in this thesis any more. This is only further confirmed by unusually high fluctuations in S.

3.3.2 Simulation Runs

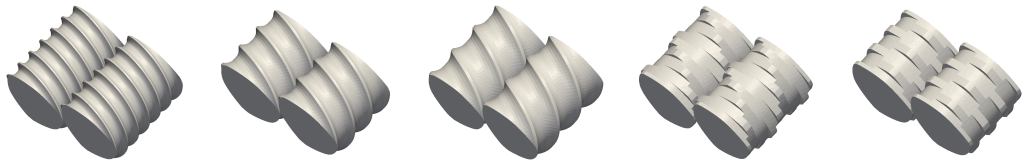

(a) C10 (b) C15 (c) C20 (d) K30 (e) K60

Figure 3.4: Overview of the investigated geometries

All five investigated elements share the same triple-flighted cross-sectional area but have a different geometry. Conveying elements (C10, C15, C20, Figure 3.4a-3.4c) are differentiated by their pitch. For example, "C10" indicates a conveying element with 10 mm pitch. Kneading elements (K30, K60, Figure 3.4d-3.4e) have different stagger angles (e.g. 30° in the case

of K30). Periodic boundary conditions at the beginning and the end of the twin-screw element call for identical cross-sectional areas on the flush side of the element. This restricts the length of a conveying element to be a multiple of the pitch. For kneading elements a similar approach is taken (Table 3.1).

Table 3.1: Geometric parameters

ID	Length [mm]	Pitch or Stagger Angle	A_{free} [mm^2]	V_{free} [mm^3]
C10	20.0	10 mm	78.660	1573.24
C15	15.0	15 mm	78.258	1173.86
C20	20.0	20 mm	78.301	1566.02
K30	19.2	30°	87.802	1685.80
K60	14.4	60°	89.902	2589.18

For each element five simulation runs with different f_z were carried out (Table 3.2). The runs with $f_z = 0$ represent a scenario where no back-pressure is applied. Contrary to that, the runs with high f_z (e.g. $f_z = 250$ for the element C10) represent a scenario where the backpressure is so high that backflow occurs.

Table 3.2: List of simulation runs: Five elements (with different p_{bg} and ρ_0) were simulated with different f_z.

geo. -	f_z [m s^{-2}]	f_z [m s^{-2}]	f_z [m s^{-2}]	f_z [m s^{-2}]	f_z [m s^{-2}]	p_{bg} [Pa]	ρ_0 [kg m^{-3}]
C10	0	65	115	160	250	2000	1250
C15	0	70	95	120	200	1400	1200
C20	0	75	90	105	125	1800	1200
K30	0	6	12	18	20	500	1150
K60	0	3	8	14	20	600	1150

Additionally to the 25 simulation runs, two simulations of C15 with a smaller gap width (C15(SG)), and one simulation of C20 with a different p_{bg} (C20(p_{bg}) were carried out (Table 3.3). The goal was to quantify the sensitivity of these parameters to the simulation results:

- p_{bg} is a modification to the EoS. If it is high, the SPH simulation is less prone to tensile instabilities, but then also the influence on the results is bigger.
- In a way, the smallest gap in the geometrical set-up determines the simulation run-time, because the space between particles Δx needs to be equal or smaller. If the particle spacing is smaller, then automatically more particles are needed to occupy the same volume, which in turn leads to longer simulations. For the C10 simulations Δx was chosen to be 0.1 mm (gap width: barrel/barrel 0.1 mm, barrel/screws 0.12 mm) instead of the 0.15 mm of previous runs.

Table 3.3: List of simulation runs: C15 with a smaller gap and C20 with a different bg

geometry	f_z	Δx	p_{bg}	ρ_0
-	[m s^{-2}]	[mm]	[Pa]	[m s^{-2}
C15(SG)	0	0.10	1400	1200
C15(SG)	120	0.10	1400	1200
C20(p_{bg})	105	0.15	1400	1200

3.3.3 Parameters

In Section 2.3 it is established that the dimensionless parameters of an extruder are not influenced by material parameters under certain flow conditions (Newtonian, creeping flow, fully filled geometries). Therefore, the following parameters are chosen: a rotational velocity n of 150 min^{-1}, a density ρ of 1000 kg m^{-3} and a viscosity η of 0.1 Pa s. This yields a Reynolds number of $Re_E = 6.65$ and ensures creeping flow.

Eqn. 3.8 is the relevant condition for limiting the fluid compressibility. A δ of 0.01 is deemed acceptable. The maximum deceleration f_z (due to flow resistance) is estimated to be 250 m s^{-2}. This yields a required c_S of 18 m s^{-1}. For all simulations a c_S of 20 m s^{-1} is chosen.

The smoothing length is determined by a common SPH convention ($h = 1.2\Delta x$). A time-step of 5.0×10^{-7} s was deemed to be sufficient for nearly all simulations. Runs which involve the C10 geometry exhibit high pressure

gradients on both sides of the flank, making it necessary to change Δt to 4.0×10^{-7} s in these cases. Naturally, the criteria for a sufficiently small time-step (Eqn. 3.23-3.25) are met, with the CFL criterion being the limiting condition by about an order of magnitude.

4 Results

In this chapter simulation results are presented and analyzed. In the first section, hydrodynamics are in the focus. The pressure- and the power characteristics are discussed and the pumping behavior is analyzed. The second section takes a closer look at distributive mixing in the elements. Tracer particle movement is shown and categorized.

4.1 Hydrodynamics

The axial velocity is of great interest in the characterization of screw elements. It is a key component in the determination of the dimensionless group V^* (Eqn. 2.1 and Eqn. 3.26). For simulation scenarios without any flow resistance (Figures 4.1a-4.1c) the axial velocities of the particles increase with the pitch. Furthermore, it can be established that axial velocities near the intermeshing region are the highest. When the flow resistance is increased axial particle velocities decrease, and various regions with back-flow are created (Figure 4.1d).

Kneading elements behave similarly, however, due to their design, which is not made for conveying, back-flow regions exist, even if there is no flow resistance (Figures 4.1e- 4.1f). Contrary to the K30 element, the forward- and back-flow regions of the K60 element are similarly sized. The screw rotation does not induce any net flow because of the neutral arrangement (stagger angles of 60°) of the flights. If the flow resistance for K30 is increased forward flowing regions diminish, back-flow regions arise and the overall mass flow decreases (Figure 4.1g).

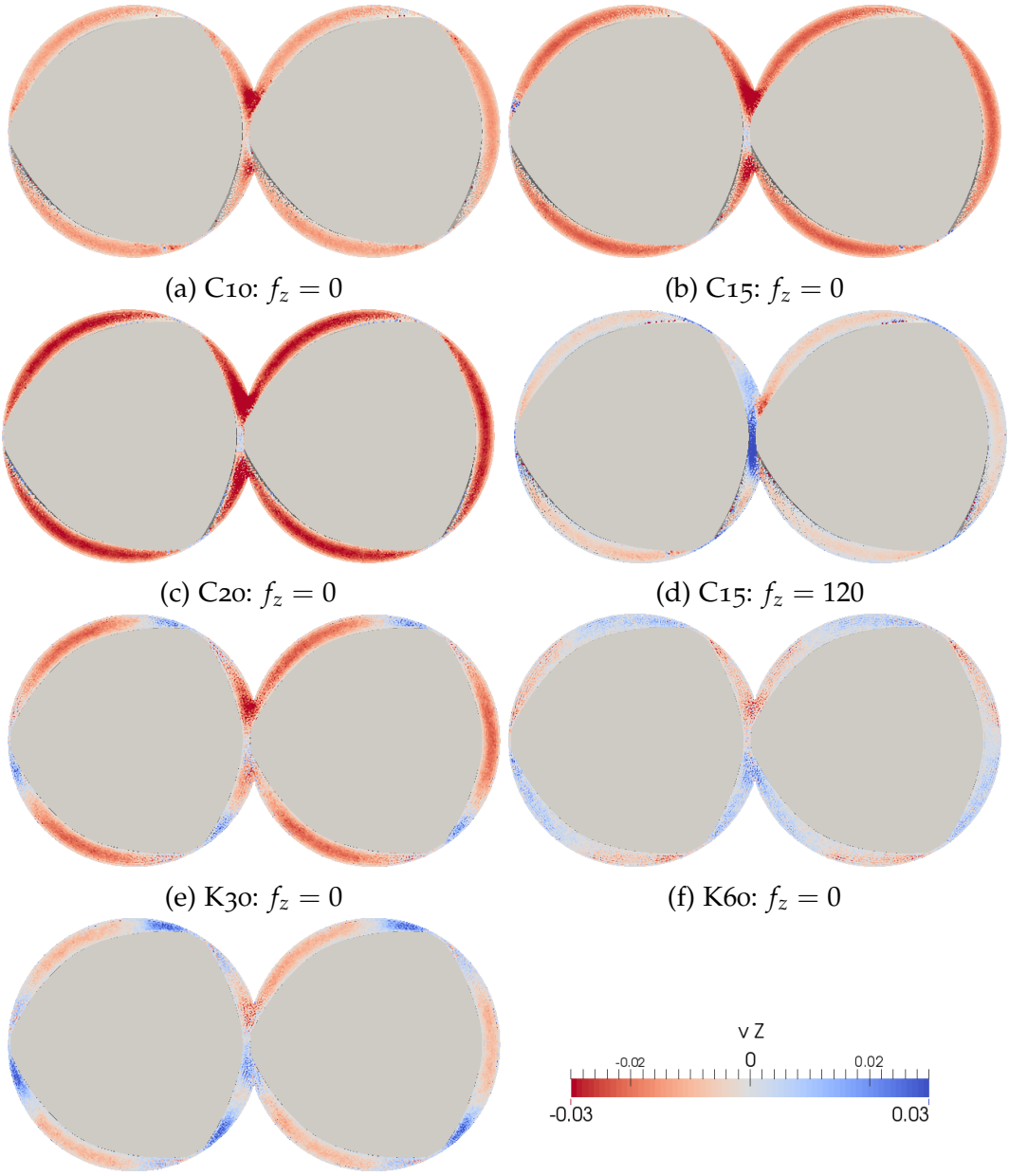

(a) C10: $f_z = 0$

(b) C15: $f_z = 0$

(c) C20: $f_z = 0$

(d) C15: $f_z = 120$

(e) K30: $f_z = 0$

(f) K60: $f_z = 0$

(g) K30: $f_z = 18$

(h) Velocity color bar (values in $\mathrm{m\,s^{-1}}$)

Figure 4.1: Axial flow velocities of different elements under various flow resistance conditions (forward flow: negative/red, backward flow: positive/blue)

4.1.1 Pressure- and Power Characteristic

The results of the flow simulations are taken, the dimensionless groups V^* and Δp^* are determined (Eqn. 2.1, 2.2, 3.26,3.27) and summarized in the pressure characteristic (Figure 4.2). All simulation points offer excellent agreement with linear fits.

The A_1 values (i.e. the intercepts with the abscissa) of the conveying elements C10, C15 and C20 rise proportionally with their pitch (10 mm, 15 mm and 20 mm). Kohlgrüber [14] states a rule of thumb for estimating A_1 in double-flighted conveying elements ($A_1 \approx 0.5 A_{free} T_S / D^3$). This estimate deviates from the obtained values (Table 4.1) about 30 %. For the simulations in this thesis a pre-factor of 0.66 yields accurate results.

A rising flow resistance automatically translates into a lower throughput. Here, conveying elements with a smaller pitch do fare better. This is reflected by their steeper slope and by their higher A_2-values (i.e. intercepts with the ordinate) (Table 4.1). The crossing point between the C10, C15 and C20 lines is merely a curios appearance and has no significance.

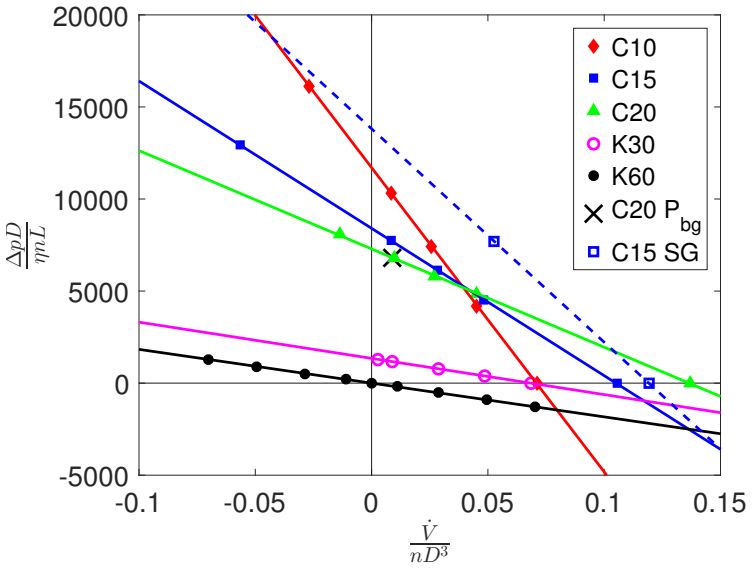

Figure 4.2: Linear fits through the obtained points to show the pressure characteristic of the investigated triple-flighted elements.

In the simulation C20(p_{bg}) a background pressure of 1400 Pa is used, instead of the 1800 Pa which are used in the corresponding simulation (C20, $f_z = 105$). The difference in the results is only marginal and can be neglected.

In contrast, the change of the gap width to 0.10 mm shows a very big influence on the pressure characteristic. Whereas A_1 is only slightly bigger, A_2 is about 60 % higher for the smaller gap geometry. It is even higher than the value for the C10 element. The influence of the gap width on the pressure characteristic is significant, which is expected.

Kneading elements are primarily designed for efficient dispersive mixing, not for pressure build-up and conveying, and it shows in their pressure characteristic. The fitted line for the K60 element intersects with the origin. A forward directed flow is only possible if a pressure gradient pushes the fluid due to the flow neutral design. Therefore, the element is not characterized by its axes intersections but by its slope A_0.

The K30 element has a different stagger angle of 30°. This design is not axially neutral. The screw rotation is able to provide a forward push. As a result the line does not pass through the origin and an A_1 and A_2 value exist. It should be noted, that although the line apparently is set off by a constant value, the slope of both fits is identical.

Table 4.1: A_1,A_2, B_1 and B_2 values for different geometries.

	A_1	A_2	B_1	B_2
C10	0.0708	11 705	0.2740	3384.1
C15	0.1051	8406	0.3647	3115.0
C20	0.1365	7289	0.4444	3220.5
K30	0.0684	1345	1.5010	1890.1
K60	$A_0 = 18332$		$B_0 = 1726.0$	
C15(SG)	0.1192	13 814	0.3815	4521.6

Similarly to the pressure characteristic, the dimensionless power numbers P^* are calculated and shown together with the corresponding throughput number V^* (Eqn 2.3, Eqn. 3.28, Figure 4.3).

The power number characterizes the screw input power which is needed for achieving a certain throughput. B_1 is the throughput that is achieved if

no power input is required. However, for that a high forward-flow inducing pressure is needed. If the throughput is even higher ($V^* > B_1$), then power is generated. Practically, these scenarios are not relevant, and therefore they are not shown on the power characteristic (Figure 4.3).

For conveying elements generally B_1 values are lower for elements with a lower pitch. As a consequence, for example, C10 needs less screw power to achieve $V^* = 0.15$ than its C15 and C20 counterparts, because the negative Δp^* value assists with the forward-flow (Figure 4.2).

Contrary to that, the lower pitch conveying elements usually have a higher B_2 value. For example, the amount of back-pressure to halt the flow ($\Delta p* = A_2$, $V^* = 0$), is higher for C10 than for C15 or C20. The power introduced into the system B_2 is also higher.

This are opposing trends, and it is not easy to say in a general way, where one trend surpasses the other. Therefore, the highest B_1 value is that of the C10 conveying element, but the lowest is the one for the C15 element and not the one for the C20 element. However, if you look at the slopes of the fitted lines, it can be clearly said that elements with higher pitches need more power input per volumetric flow unit.

Same as in the pressure characteristic, the simulation with a changed p_{bg} parameter only has a negligible influence on P^*. Also similar to the pressure characteristic discussed before, the power characteristic for the C15 element with smaller gaps generally requires more screw input power. For instance, the B_1 value is about 45 % higher.

The kneading element K60 does not contribute to conveying at all. This is why its power consumption is independent of the throughput and thus a constant value B_0 (Table 4.1). Contrary to that, K30 has a slight conveying nature. The higher the opposing pressure the more power needs to be consumed.

4.1.2 Pumping Behavior

With the obtained A_1, A_2, B_1 and B_2 values the pumping power and the pumping efficiency can be calculated easily (Eqn. 2.8, 2.10, 2.13).

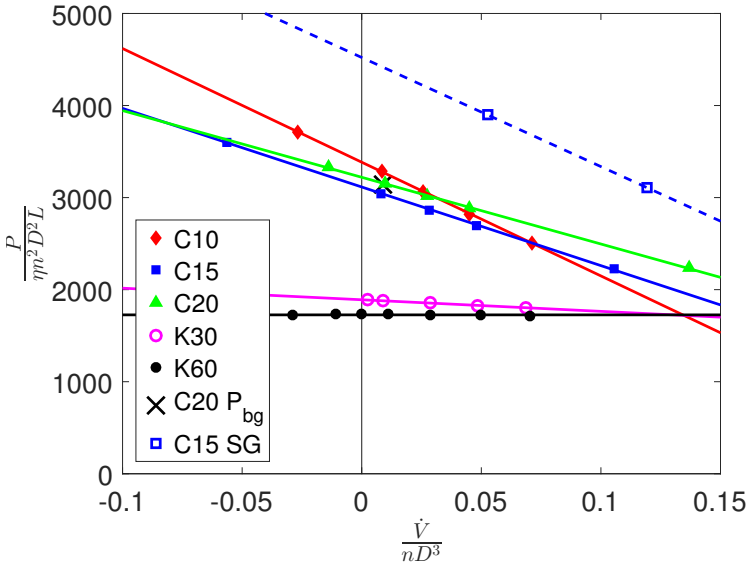

Figure 4.3: Linear fits through the obtained points to show the power characteristic of the investigated triple-flighted elements.

The linear pressure characteristic leads to a parabolic curve for P^*_{Pump} (Figure 4.4a). At $V^* = 0$, there is no throughput and therefore no pumping power. At $V^* = A_1$, there is per definition no pressure difference, which results again in zero pumping power. The parabolic nature requires P^*_{Pump} to peak at $V^* = A_1/2$. Conveying elements with a higher pitch have the potential to also achieve a higher maximum pumping power. The highest P^*_{Pump} values, however, are associated with the small gap simulation of C15, because of its better pressure build-up. The Kneading element K60 has no conveying capability. Even the slightest flow resistance inverses the throughput. Therefore, the pumping power for the K60 element is always negative. The K30 element with its 30° stagger angle shows a pumping behavior similar to conveying elements.

It is apparent that screw elements are not designed to be efficient pumps. The maximum achievable efficiency factor is little over 10 %. Again, the K60 element with its entirely negative η_e stands out.

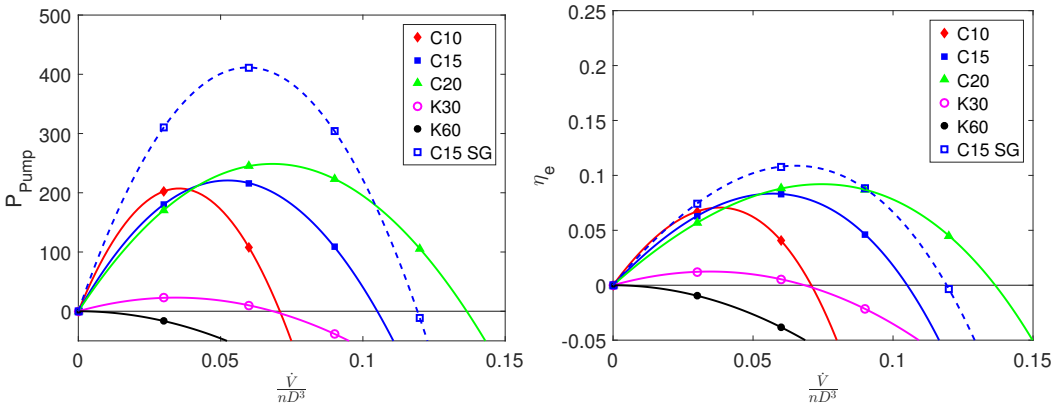

(a) Pumping power (b) Pumping efficiency

Figure 4.4: Pumping power and pumping efficiency calculated for different screw elements using A_1, A_2, B_1 and B_2 values.

4.2 Mixing

To gauge the mixing performance of elements in the axial direction the Axial tracer is tracked for several rotations (Figure 4.5). A moving front can be observed. At $N = 0$ the bottom half consists purely of tracer particles. Then, at $N = 1$ the tracer traveled in the flow direction (downwards), crossed the bottom and then the top boundary (due to the periodic boundary conditions). From $N = 2$ to $N = 4$ the moving front travels further in the flow direction until it catches up with the longer residing tracer particles. After that, from $N = 5$ to $N = 7$, the tracer seems to be perfectly mixed to the naked eye, however, that is not true.

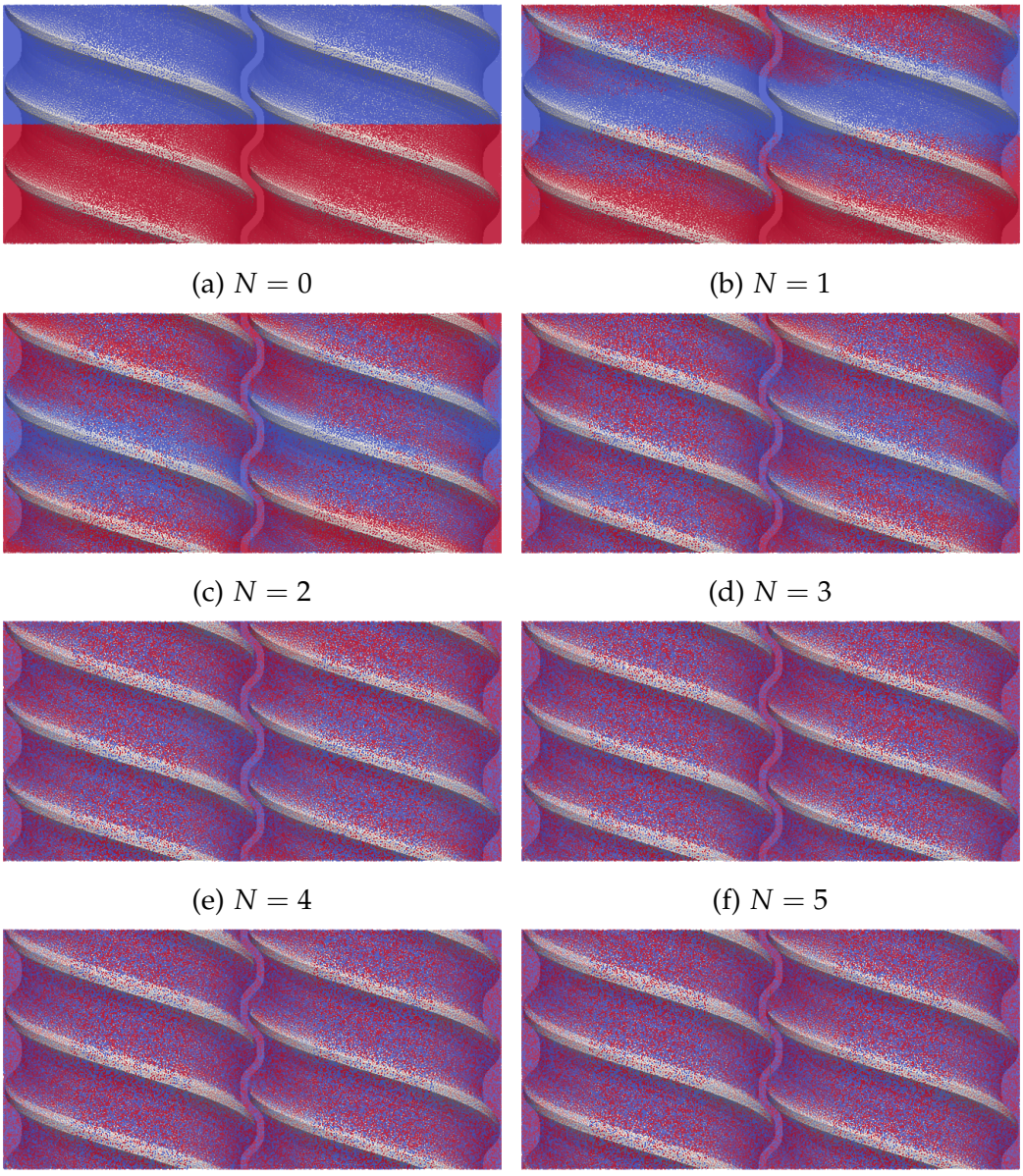

(a) $N = 0$ (b) $N = 1$

(c) $N = 2$ (d) $N = 3$

(e) $N = 4$ (f) $N = 5$

(g) $N = 6$ (h) $N = 7$

Figure 4.5: Evolution of the Axial Tracer (C15, $f_z = 0$)

The logarithmic plots (Figure 4.6) show that at higher rotations mixing still occurs, albeit at a lower rate. Generally, it can be differentiated between initial mixing with a faster tracer distribution (k_1, k_2) and long-term mixing where the tracer is distributed slower (k_3). In the simulations long-term mixing can be observed, when a tracer front cannot be distinguished anymore (e.g. Figure 4.5f-4.5h). For shorter elements the shift to long-term mixing happens sooner compared to longer elements (e.g. C15, $L = 15\,\text{mm}$, Figure 4.6a; C20, $L = 20\,\text{mm}$, Figure 4.6b).

However, real TSE elements as a whole – segmented or otherwise – are much longer than the simulated parts. So long, in fact, that the length does not matter for the flow. This is also implied by the periodic boundary conditions which create an infinitely long element. Therefore, for practical considerations the long-term mixing rate k_3 is the distributive mixing defining parameter. However, for quantitative comparisons between different elements k_1 and k_2 can be used as well. Note, that all mixing rates in Figure 4.6 are higher for the C15 element.

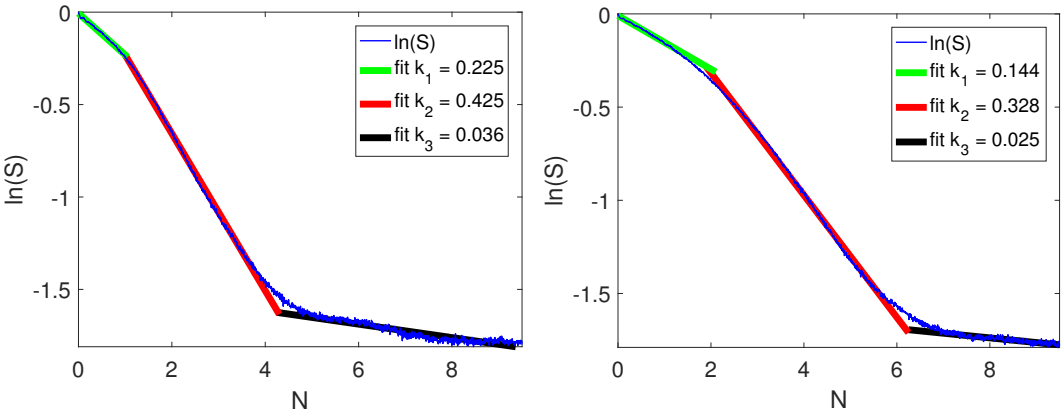

(a) C15, $f_z = 70$ (b) C20, $f_z = 75$

Figure 4.6: Logarithmic plot of the Segregation S (Eqn. 2.15) and fits of the kinetic segregation model (Eqn. 2.16)

With the Cross-tracer the distribution of tracer particles from one screw to the other is measured. Similarly to the Axial tracer a moving front can be observed for a while (from $N = 0$ to $N = 4$ in Figure 4.7). Afterwards, the visible front disappears and long-term mixing sets in.

The Quarter-tracer (Figure 4.8) is able to portray the combined effects of axial-mixing and cross-mixing. Because, both effects play a role, the shift from short-term to long-term mixing is not as sharp.

The Axial, Cross and Quarter tracer are also applicable for kneading elements. However, due to their nature, axial distribution progresses slower. This can be demonstrated for K60 (Figure 4.9). If there is no flow resistance (i.e. $f_z = 0$), then no axial mixing is observed.

The Quarter tracer is able to portray the effect of axial and cross mixing. Usually, the corresponding mixing rate is found to lie quantitatively in between (Figure 4.10).

A rise in axial velocities should also enhance axial mixing. This is reflected when short-term mixing exponents are plotted versus the throughput (Figure 4.11b). Clearly, k_1 values are higher for higher throughput numbers. One would expect conveying elements to have a better mixedness along the axis compared to kneading elements but this is not the case for k_1 values. Considering long-term mixing effects, however, offers a clearer view. Here (Figure 4.11c), conveying elements have a superior mixing performance compared to the kneading elements.

For conveying elements the cross mixing ability is sinking with rising throughput numbers (Figure 4.11a). This is also true for long-term mixing exponents (Figure 4.11d). In both cases kneading elements consistently offer a better cross mixing performance.

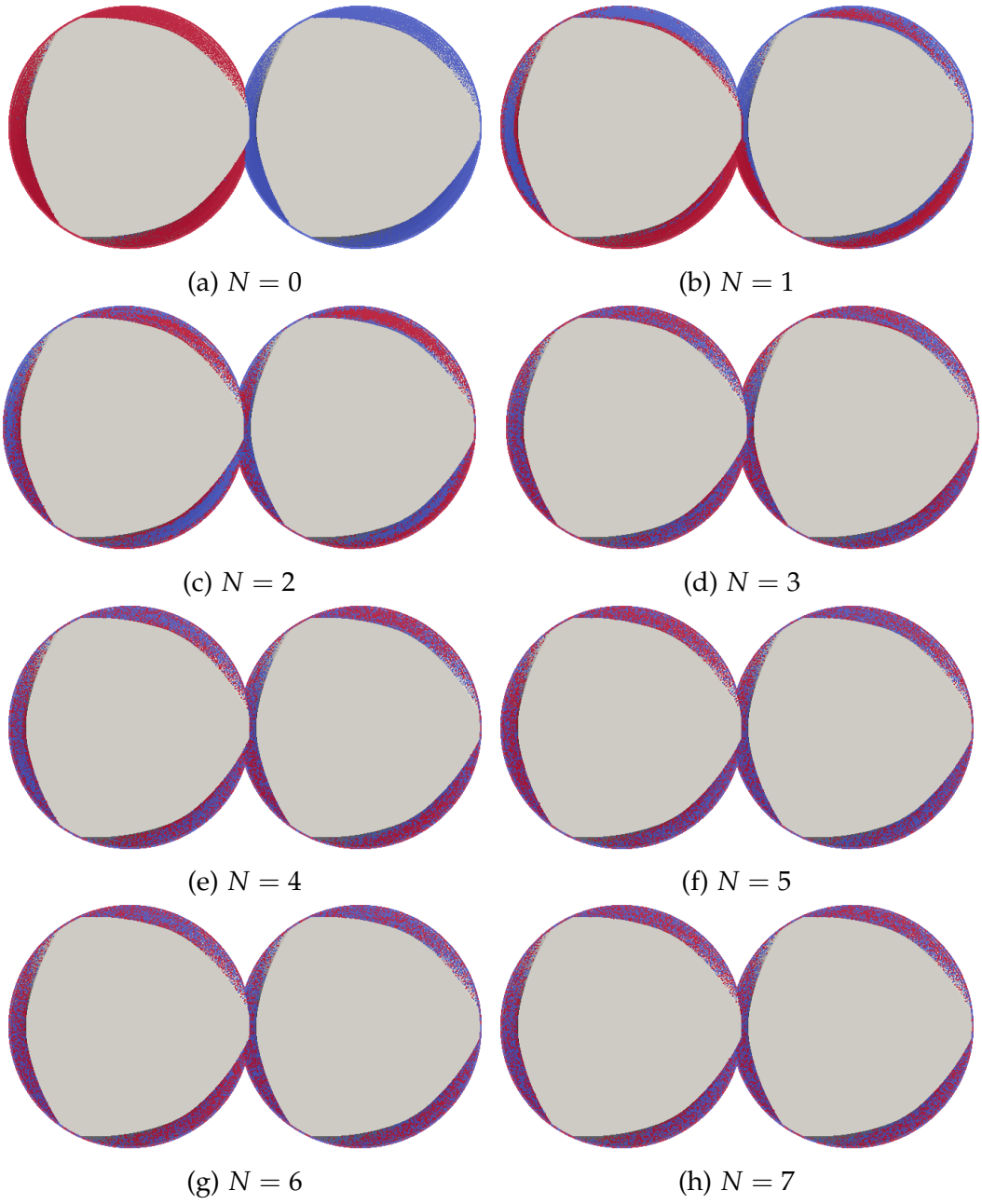

(a) $N = 0$ (b) $N = 1$

(c) $N = 2$ (d) $N = 3$

(e) $N = 4$ (f) $N = 5$

(g) $N = 6$ (h) $N = 7$

Figure 4.7: Evolution of the Cross Tracer (C15, $f_z = 0$, counterclockwise rotation)

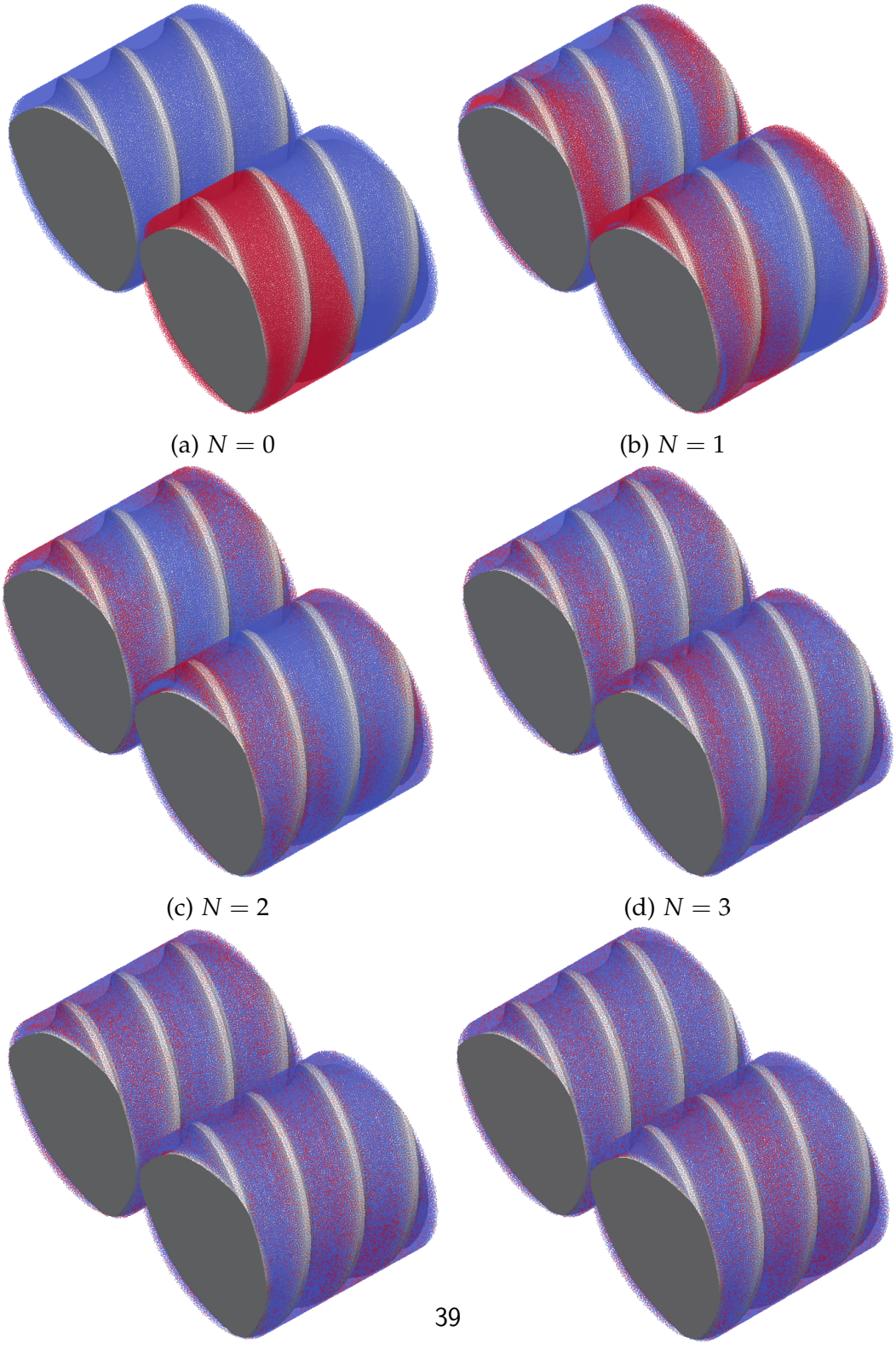

(a) $N = 0$ (b) $N = 1$

(c) $N = 2$ (d) $N = 3$

(e) $N = 4$ (f) $N = 5$

Figure 4.8: Evolution of the Quarter Tracer (C15, $f_z = 0$)

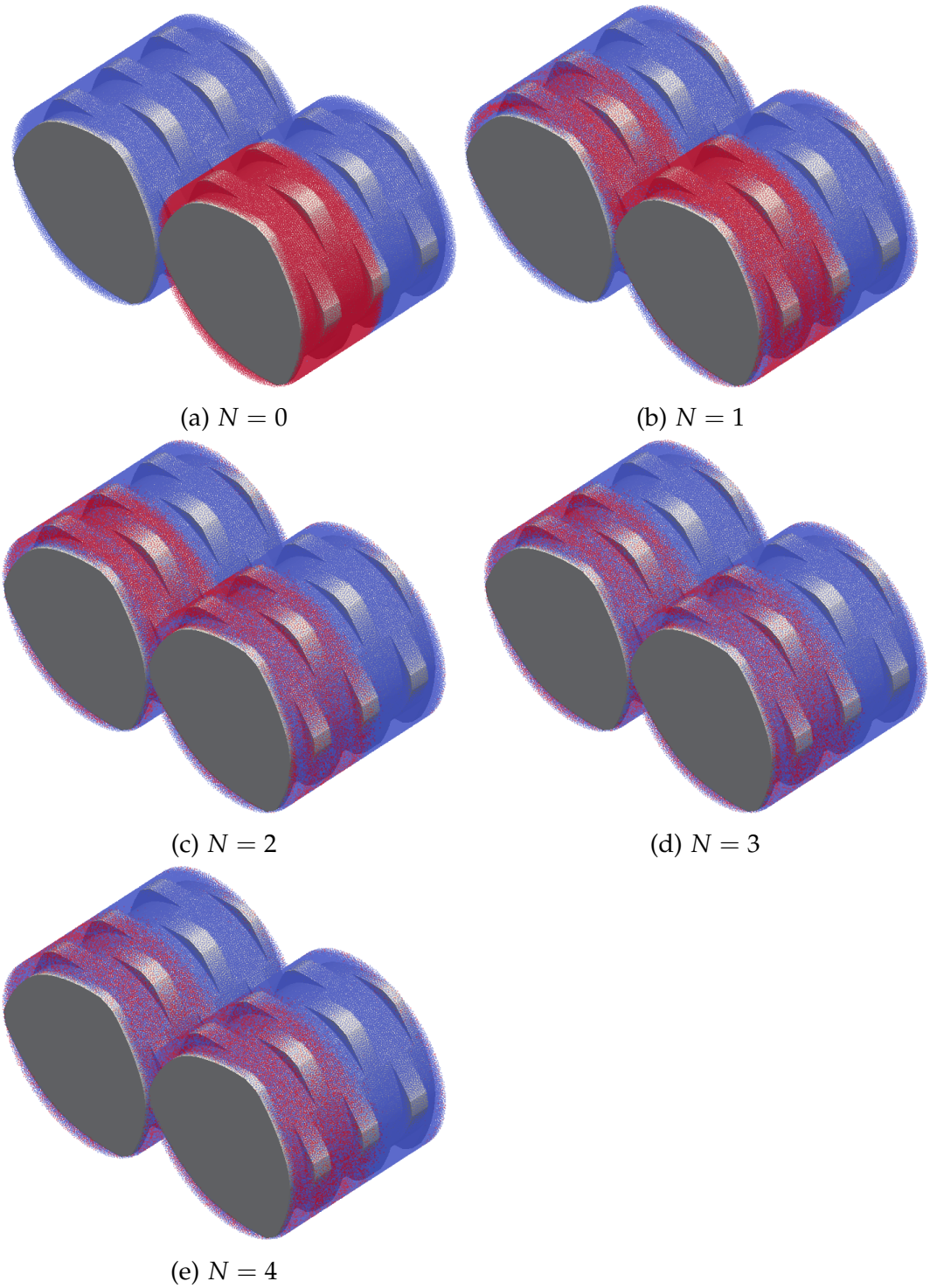

(a) $N = 0$ (b) $N = 1$

(c) $N = 2$ (d) $N = 3$

(e) $N = 4$

Figure 4.9: Evolution of the Quarter Tracer (K60, $f_z = 0$)

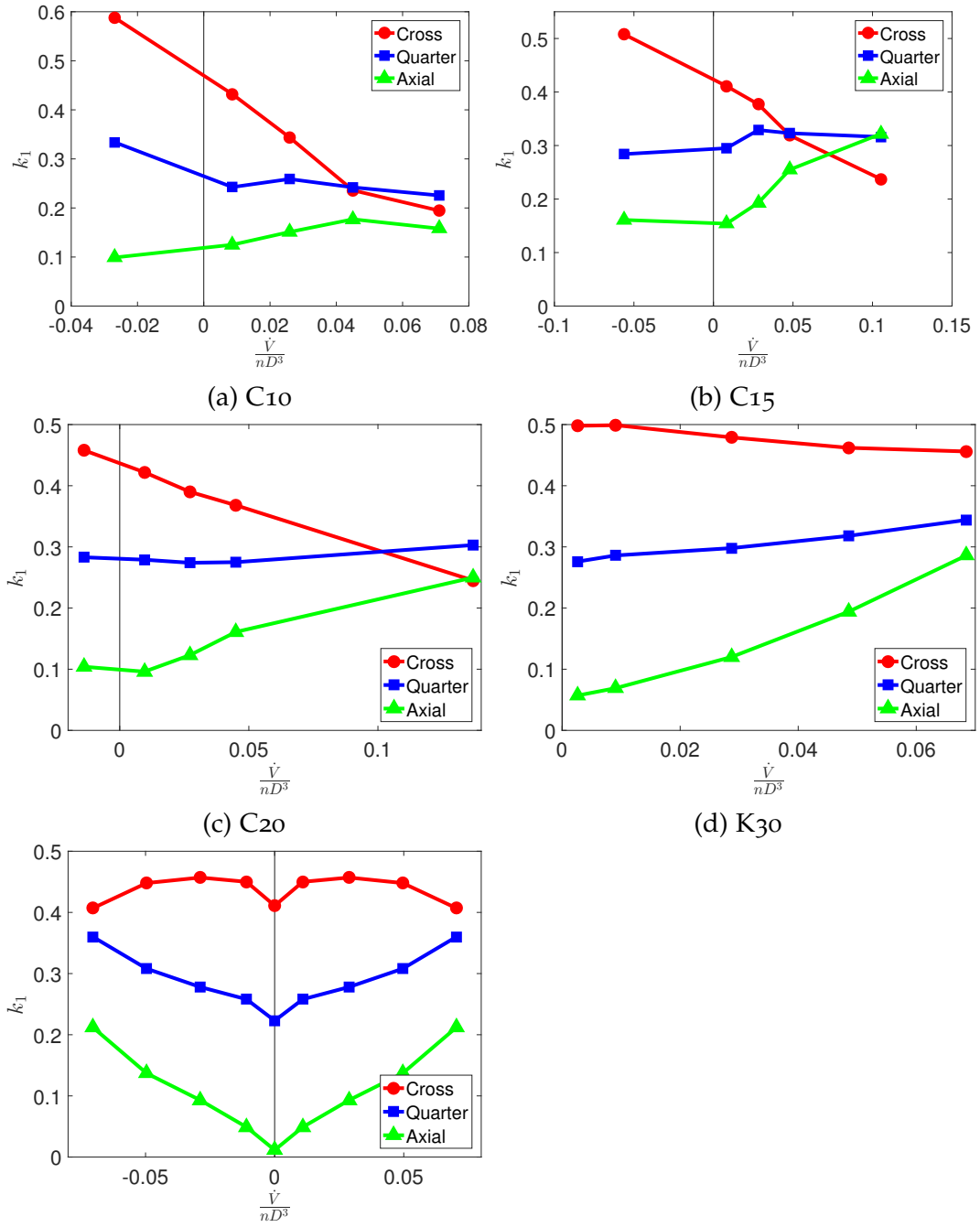

(a) C10

(b) C15

(c) C20

(d) K30

(e) K60

Figure 4.10: Overview of k_1-values for different tracers per element.

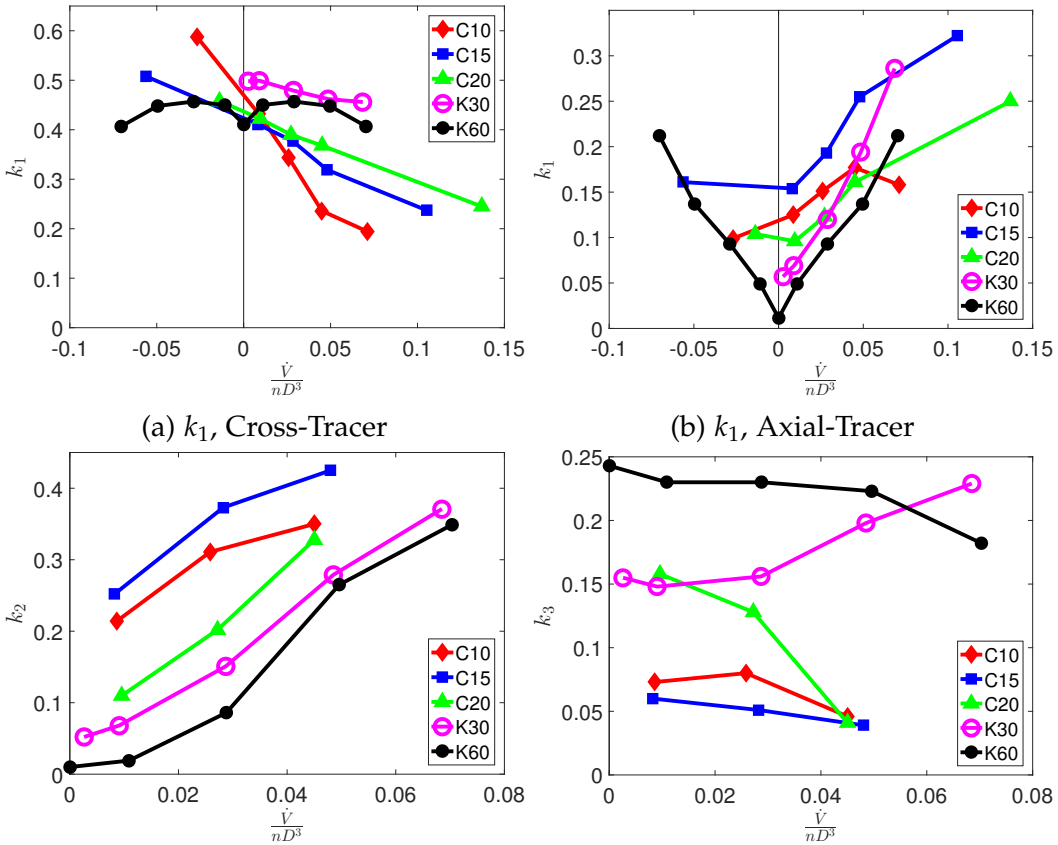

(a) k_1, Cross-Tracer

(b) k_1, Axial-Tracer

(c) k_2, Axial tracer

(d) k_3, Cross tracer

Figure 4.11: Fitted segregration exponents k for various tracer types

4.3 Comparison of Triple-Flighted Elements to Double Flighted Elements

In their soon to be published paper Eitzlmayr, Matic, and Khinast [8] investigated the pressure and power characteristic of double flighted (DF) elements from a MICRO27 TSE (barrel diameter: 27.6 mm, gap width 0.3 mm) . Their results are compared with the pressure and power characteristic for the triple flighted (TF) NANO16 elements (Figure 4.12).

To isolate the effect that the number of flights has on pressure and power characteristic, all other parameters should be geometrically similar. The gap to barrel diameter ratios (0.011 for MICRO27 elements, and 0.009 for NANO16 elements) are assumed to be similar. For conveying elements geometrical similarity means an equal pitch to barrel diameter ratio (T_S/D).

The TF-C15 element and the DF-C30 element have similar T_S/D ratios. Generally, a better pressure build-up can be attributed to the TF-C15 element (Figure 4.12a). Interestingly enough, the DF-C15 element and the TF-C20 element have a similar pressure characteristic.

The power characteristic shows the same behavior (Figure 4.12b). TF-C15 shows a higher power input than DF-C30. The lines for DF-C15 and TF-C20 nearly overlap.

The pressure characteristic of kneading elements (Figure 4.12c) shows the same slope for elements with the same number of flights.

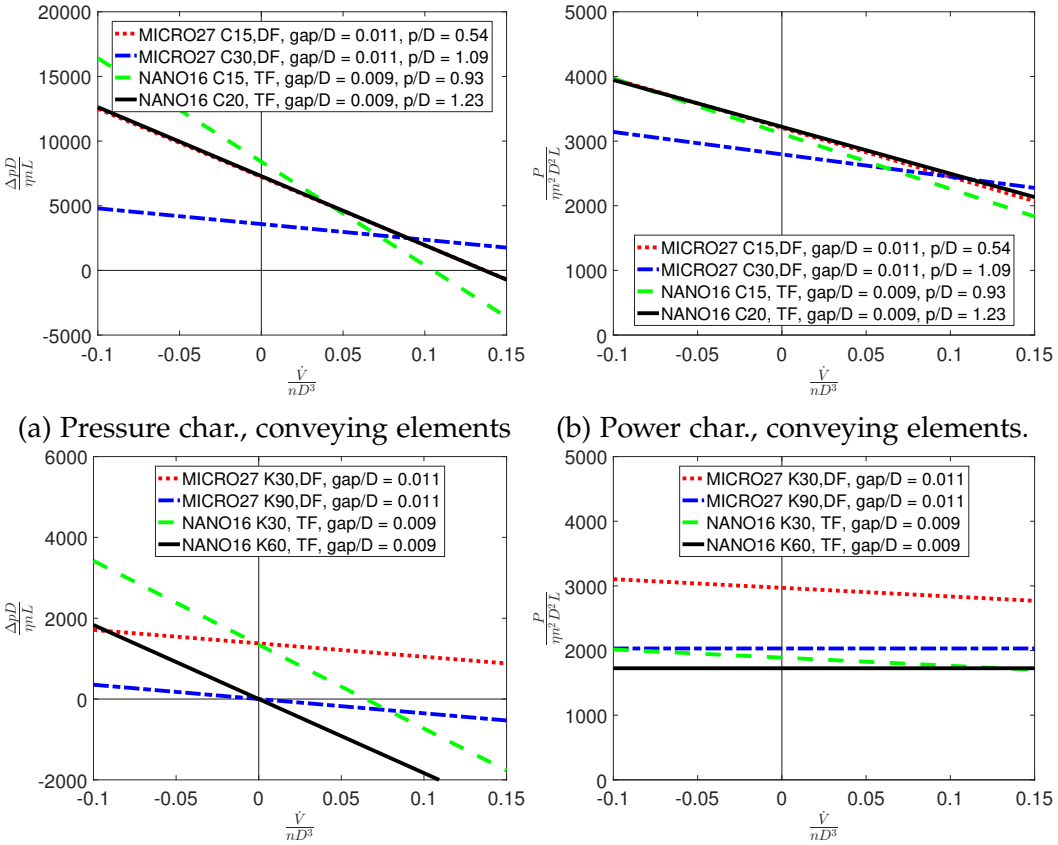

(a) Pressure char., conveying elements (b) Power char., conveying elements.

(c) Pressure char., Kneading elements (d) Power char., Kneading elements

Figure 4.12: Differences in pressure- and power characteristic for double- and triple-flighted elements (Conveying and Kneading elements as used in the NANO16 and MICRO27 extruder)

5 Summary and Conclusions

The hydrodynamic flow of a highly viscous, Newtonian fluid through three conveying and two kneading TSE elements – all of them triple-flighted – was investigated. The used method of SPH allowed for efficient particle tracking and therefore a characterization of mixing behavior.

The obtained pressure characteristics identify the pressure build-up capabilities of all geometrically similar elements. In the same way, the obtained power characteristic identifies the necessary power input via the rotating twin-screws. Both lines are defined by their parameters A_1, A_2, B_1 and B_2, which can be used in a 1-D model to also account for the interactions between the screws.

In terms of pressure build-up and and power input conveying elements achieve consistently higher values than kneading elements. However, kneading elements shine when cross mixing is desired. There, they offer good results over a wide throughput range. The obtained segregation exponents for long-term mixing can also be used in a 1-D model to estimate the mixedness along the extruder.

The comparison of pressure- and power characteristic between triple-flighted and double-flighted elements shows how much higher the pressure-build up and the power input of triple flighted elements can be. Furthermore, it shows that triple-flighted elements with practically the same pressure- and power characteristic exist. TSE vendors can make use of this information and tailor their screw portfolio to allow for an easier process transfer between the different production stages.

It is safe to say that SPH will continue to play a significant role in the simulation of flow behavior for extrusion elements. Its disadvantages – namely high computational effort if the gap in extruder elements is fully

resolved – may be resolved in the future, opening up further possibilities for SPH:

- Incompressible formulations may lead to faster computation times because the time-stepping criteria do not depend on the speed of sound anymore. [5]
- GPU computing, already extensively used for CFD and Lattice-Boltzmann methods, will also leave its impression on SPH and further decrease computational effort.
- Particle splitting is a promising technique that may allow to enhance the resolution locally, cutting down the overall particle number needed, and increasing the performance. [13]
- With these speed enhancements additional functionality will become feasible for extruder element simulation (e.g. non-Newtonian fluid behavior, energy transport).

Appendix

List of Tables

Bibliography

[1] S. Adami, X. Y. Hu, and N. A. Adams. "A transport-velocity formulation for smoothed particle hydrodynamics." In: *J. Comput. Phys.* 241 (2013), pp. 292–307. ISSN: 00219991. DOI: 10.1016/j.jcp.2013.01.043 (cit. on p. 20).

[2] Jörg Breitenbach. "Melt extrusion: from process to drug delivery." In: *Eur. J. Pharm. Biopharm.* 54.2 (2002), pp. 107–117. DOI: 10.1016/S0939-6411(02)00061-9 (cit. on p. 1).

[3] Hongfei Cheng and I C A Manas-zloczower. "Distributive Mixing in Conveying Elements of a ZSK-53 Co-rotating Twin Screw Extruder." In: *Polym. Eng. Sci.* 38.6 (1998), pp. 926–935 (cit. on p. 12).

[4] P W Cleary, M Prakash, and J Ha. "Novel applications of smoothed particle hydrodynamics (SPH) in metal forming." In: *J. Mater. Process. Technol.* 177 (2006), pp. 41–48. DOI: 10.1016/j.jmatprotec.2006.03.237 (cit. on p. 13).

[5] Sharen J Cummins and Murray Rudman. "An SPH Projection Method." In: *J. Comput. Phys.* 607 (1999), pp. 584–607 (cit. on p. 46).

[6] Andreas Eitzlmayr and Johannes Khinast. "Co-rotating twin-screw extruders: Detailed analysis of conveying elements based on smoothed particle hydrodynamics. Part 1: Hydrodynamics." In: *Chem. Eng. Sci.* 134 (2015), pp. 861–879. ISSN: 00092509. DOI: 10.1016/j.ces.2015.04.055. URL: http://dx.doi.org/10.1016/j.ces.2015.05.035 (cit. on pp. 7, 14).

[7] Andreas Eitzlmayr, Gerold Koscher, and Johannes Khinast. "A novel method for modeling of complex wall geometries in smoothed particle hydrodynamics." In: *Comput. Phys. Commun.* 185.10 (2014), pp. 2436–2448. ISSN: 00104655. DOI: 10.1016/j.cpc.2014.05.014. URL: http://dx.doi.org/10.1016/j.cpc.2014.05.014 (cit. on pp. 2, 13, 21).

[8] Andreas Eitzlmayr, Josip Matic, and Johannes Khinast. "Analysis of Flow and Mixing in Screw Elements of Co-Rotating Twin-Screw Extruders via SPH." 2016 (cit. on p. 42).

[9] Andreas Eitzlmayr et al. "Mechanistic modeling of modular co-rotating twin-screw extruders." In: *Int. J. Pharm.* 474.1-2 (2014), pp. 157–176. ISSN: 18733476. DOI: 10.1016/j.ijpharm.2014.08.005. URL: http://dx.doi.org/10.1016/j.ijpharm.2014.08.005 (cit. on pp. 4, 20).

[10] Georg C. Ganzenmüller, Martin O. Steinhauser, and Paul Van Liedekerke. *The implementation of Smooth Particle Hydrodynamics in LAMMPS. A guide to the SPH-USER package*. 2011 (cit. on p. 19).

[11] R. A. Gingold and J. J. Monaghan. "Kernel estimates as a basis for general particle methods in hydrodynamics." In: *J. Comput. Phys.* 46.3 (1982), pp. 429–453. ISSN: 10902716. DOI: 10.1016/0021-9991(82)90025-0 (cit. on p. 13).

[12] J. F. Hetu and F. Ilinca. "Immersed boundary finite elements for 3D flow simulations in twin-screw extruders." In: *Comput. Fluids* 87 (2013), pp. 2–11. ISSN: 00457930. DOI: 10.1016/j.compfluid.2012.06.025. URL: http://dx.doi.org/10.1016/j.compfluid.2012.06.025 (cit. on p. 13).

[13] S Kitsionas and A P Whitworth. "Smoothed Particle Hydrodynamics with particle splitting , applied to self-gravitating collapse." In: *Mon. Not. R. Astron. Soc.* February (2008), pp. 1–9. arXiv: 0203057v1 [arXiv:astro-ph] (cit. on p. 46).

[14] Klemens Kohlgrüber. *Der gleichläufige Doppelschneckenextruder*. München: Carl Hanser Verlag, 2008. ISBN: 978-3-446-41252-1 (cit. on pp. 6, 12, 30).

[15] P. M. C. Lacey. "Developments in the theory of particle mixing." In: *J. Appl. Chem.* 4.5 (1954), pp. 257–268. ISSN: 1934-998X. DOI: 10.1002/jctb.5010040504 (cit. on p. 11).

[16] M. B. Liu and G. R. Liu. *Smoothed particle hydrodynamics (SPH): An overview and recent developments*. Vol. 17. 1. 2010, pp. 25–76. ISBN: 1183101090. DOI: 10.1007/s11831-010-9040-7 (cit. on p. 19).

[17] J Monaghan. "SPH without a Tensile Instability." In: *J. Comput. Phys.* 159.2 (2000), pp. 290–311. ISSN: 00219991. DOI: 10.1006 (cit. on p. 18).

[18] J. J. Monaghan and J. B. Kajtar. "SPH particle boundary forces for arbitrary boundaries." In: *Comput. Phys. Commun.* 180.10 (2009), pp. 1811–1820. ISSN: 00104655. DOI: 10.1016/j.cpc.2009.05.008. URL: http://dx.doi.org/10.1016/j.cpc.2009.05.008 (cit. on p. 21).

[19] J.J. Monaghan. *Simulating free surface flows with SPH*. 1994. DOI: 10.1006/jcph.1994.1034. URL: http://www.sciencedirect.com/science/article/pii/S0021999184710345 (cit. on p. 13).

[20] J.J. Monaghan. "SMOOTHED PARTICLE HYDRODYNAMICS." In: *Annu. Rev. Astron. Astrophys.* 30 (1992), pp. 543–574. ISSN: 0066-4146. URL: http://adsabs.harvard.edu/full/1992ARA%7B%5C&%7DA..30..543M (cit. on pp. 14–17).

[21] J.J. Monaghan and A Kos. "Solitary Waves on a Cretan Beach." In: *J. Waterw. Port, Coastal, Ocean Eng.* 125.May/June (1999), pp. 145–154 (cit. on p. 13).

[22] Joseph P. Morris, Patrick J. Fox, and Yi Zhu. "Modeling Low Reynolds Number Incompressible Flows Using SPH." In: *J. Comput. Phys.* 136 (1997), pp. 214–226. ISSN: 00219991. DOI: 10.1006/jcph.1997.5776. URL: http://www.sciencedirect.com/science/article/pii/S0021999197957764 (cit. on pp. 16, 18, 20).

[23] Matthias Müller, David Charypar, and Markus Gross. "Particle-Based Fluid Simulation for Interactive Applications." In: *Eurographics/SIGGRAPH Symp. Comput. Animat.* (2003), pp. 154–160 (cit. on p. 13).

[24] Edward L Paul. *Handbook of industrial mixing : science and practice*. Hoboken, New Jersey: John Wiley & Sons, Inc., 2004. ISBN: 0-471-26919-0 (cit. on p. 9).

[25] Juri Pawlowski. *Die Ähnlichkeitstheorie in der physikalisch-technischen Forschu*. Springer Berlin Heidelberg, 1971. ISBN: 978-3-642-65096-3. DOI: 10.1007/978-3-642-65095-6 (cit. on p. 6).

[26] R.A. Lai-Fook, A. Senouci and A. C. Smith. "Pumping Characteristics of Self-Wiping Twin Screw Extruders – A Theoretical and Experimental Study on Biopolymer Extrusion." In: *Polym. Eng. Sci.* 29.7 (1989), pp. 433–440 (cit. on p. 12).

[27] C Rauwendaal. *Polymer Extrusion*. 4th ed. Munich: Carl Hanser Verlag, 2001. ISBN: 978-3-446-21774-4 (cit. on p. 12).

[28] Arash Sarhangi Fard and Patrick D. Anderson. "Simulation of distributive mixing inside mixing elements of co-rotating twin-screw extruders." In: *Comput. Fluids* 87 (2013), pp. 79–91. ISSN: 00457930. DOI: 10.1016/j.compfluid.2013.01.030. URL: http://dx.doi.org/10.1016/j.compfluid.2013.01.030 (cit. on p. 13).

[29] Hadi Sobhani et al. "Non-Isothermal modeling of a non-newtonian fluid flow in a twin screw extruder using the fictitious domain method." In: *Macromol. Theory Simulations* 22.9 (2013), pp. 462–474. ISSN: 10221344. DOI: 10.1002/mats.201300110 (cit. on p. 13).

[30] Volker (Max-Planck-Institut für Astrophysik) Springel. "Smoothed Particle Hydrodynamics in Astrophysics." In: *Annu. Rev. Astron. Astrophys.* 48 (2016), 319:430. arXiv: arXiv:1109.2219v1 (cit. on p. 13).

[31] Daniel Treffer and Simone Schrank. *Pellet Production by Hot Melt Extrusion and Die Face Pelletising*. 2013. URL: http://www.pssrc.org/component/k2/89 (visited on 09/05/2016) (cit. on p. 1).

[32] R Vacondio, P Mignosa, and S Pagani. "Advances in Water Resources 3D SPH numerical simulation of the wave generated by the Vajont rockslide." In: *Adv. Water Resour.* 59 (2013), pp. 146–156. ISSN: 0309-1708. DOI: 10.1016/j.advwatres.2013.06.009. URL: http://dx.doi.org/10.1016/j.advwatres.2013.06.009 (cit. on p. 13).